

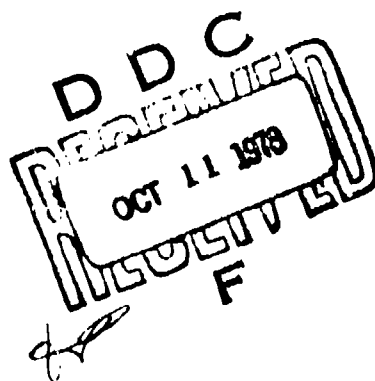
LEVEL

2

NPS-69PS-78-004

NAVAL POSTGRADUATE SCHOOL

Monterey, California



FILE COPY
DDC

THE EFFECT OF FLOW STRUCTURE ON
CORROSION: CIRCLING-FOIL STUDIES ON
90/10 COPPER-NICKEL, AND HYDRODYNAMIC
MODELING OF THE EROSION-CORROSION PROCESS

G. Leumer, R. P. Schack
K. J. Graham, and J. Perkins

May 1978

Technical Report No. 8
To the Office of Naval Research
Contract No. N00014-78-WR-80105
NR-025-120

Approved for public release; distribution unlimited.
Reproduction in whole or in part is permitted for any purpose of the
United States Government.

NAVAL POSTGRADUATE SCHOOL
Monterey, California

Rear Admiral T. F. Dedman
Superintendent

Jack R. Borsting
Provost

The work reported herein was supported by the Office of Naval Research,
Metallurgy Program Office, Code 47i, Arlington, VA, 22217, through Contract
No. N00014-78-WR-80105, NR-036-120.

Reproduction of all or part of this report is authorized.

This report was prepared by:

Jeff Perkins
Jeff Perkins
Associate Professor of
Mechanical Engineering

G. Leumer
G. Leumer

R. P. Schack
R. P. Schack

K. J. Graham
K. J. Graham

Reviewed by:

P. J. Marto
Paul J. Marto, Chairman
Department of Mechanical Engineering

William M. Tolles
William Tolles
Dean of Research

UNCLASSIFIED

SECURITY CLASSIFICATION OF THIS PAGE (When Data Entered)

REPORT DOCUMENTATION PAGE		READ INSTRUCTIONS BEFORE COMPLETING FORM
1. REPORT NUMBER NPS-69PS-78-004	2. GOVT ACCESSION NO.	3. RECIPIENT'S CATALOG NUMBER
4. TITLE (and subtitle) THE EFFECT OF FLOW STRUCTURE ON CORROSION: CIRCLING-FOIL STUDIES ON 90/10 COPPER-NICKEL, AND HYDRODYNAMIC MODELING OF THE EROSION-CORROSION PROCESS		5. TYPE OF REPORT & PERIOD COVERED Interim, 9/77 to 5/78
6. AUTHOR(S) G. Leumer, R. P. Schack, K. J. Graham J. Perkins		7. PERFORMING ORG. REPORT NUMBER Technical Report No. 8
8. CONTRACT OR GRANT NUMBER(S) N00014-78-WR-80105, NR-036-120		9. PROGRAM ELEMENT, PROJECT, TASK AREA & WORK UNIT NUMBERS Program Element : 61153N Project: RROZ 08-01
10. CONTROLLING OFFICE NAME AND ADDRESS Office of Naval Research, Metallurgy Program Office, Code 471, Arlington, VA 22217		11. REPORT DATE May 1978
12. MONITORING AGENCY NAME & ADDRESS (if different from Controlling Office) (16) RR 03, 3, 28 / (17) RR 03, 2, 08 02		13. NUMBER OF PAGES
14. DISTRIBUTION STATEMENT (of the abstract entered in Block 02, if different from Report) Approved for public release; distribution unlimited. Reproduction in whole or in part is permitted for any purpose of the United States Government.		15. SECURITY CLASS. (of this report)
		16a. DECLASSIFICATION/DOWNGRADING SCHEDULE
17. DISTRIBUTION STATEMENT (of the abstract entered in Block 02, if different from Report) (18) NPS-69PS-78-004, NPS-TR-8 /		
18. SUPPLEMENTARY NOTES (19) Technical rept.		
19. KEY WORDS (Continue on reverse side if necessary and identify by block number) velocity effects, corrosion rates, flow structure, fluid flow, turbulence, marine corrosion, copper-nickel alloys		
20. ABSTRACT (Continue on reverse side if necessary and identify by block number) The effects of turbulent flow on the corrosion behavior of 90/10 Cu-Ni were studied experimentally in synthetic seawater electrolyte, using a circling foil apparatus at relative velocities up to about 6 m/sec. The flow field at the specimen surface was characterized by anemometric methods. Corrosion rates were determined by direct weight loss and by several electrochemical methods, including the linear polarization method and from Tafel plots; also zero resistance ammeter measurements were made on galvanic couples. Consideration was given to the question of the appropriate analytical approach to velocity (fluid flow)		

UNCLASSIFIED

SECURITY CLASSIFICATION OF THIS PAGE(When Data Entered)

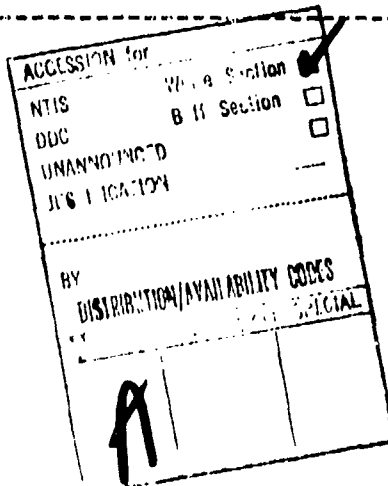
effects on corrosion processes. The contribution of convective diffusion is considered dominant over the velocity range studied, and the rate of eddy diffusivity (fine flow structure effects on mass transport) is described. The separate electrochemical and mechanical influences of high-intensity turbulent flows are considered.

UNCLASSIFIED

SECURITY CLASSIFICATION OF THIS PAGE(When Data Entered)

Table of Contents

INTRODUCTION -----	1
EXPERIMENTAL -----	2
Linear Polarization Method-----	6
Potentiodynamic Polarization Curves -----	7
Zero-Resistance Ammeter -----	7
Hot-Film Anemometry -----	8
RESULTS -----	12
1. Effect of Velocity on Corrosion Rates-----	12
WL and LPM-----	12
Polarization Curves-----	13
ZRA-----	14
2. Corrosion Products and Surface Morphology-----	14
DISCUSSION: HYDRODYNAMIC CONSIDERATIONS IN CORROSION-----	19
1. Boundary Layers in Turbulent Flow-----	19
2. Mass Transfer Considerations-----	23
3. Possible Parameters for Corrosion Rate Correlations-----	29
SUMMARY AND CONCLUSIONS-----	33
REFERENCES-----	37
LIST OF TABLES-----	39
LIST OF FIGURES-----	45



INTRODUCTION

When the corrosion rate of a metal is higher in a flowing electrolyte than in a stagnant system, the process is called erosion-corrosion. Erosion-corrosion is distinguished from simple erosion. Whereas erosion is a purely mechanical effect, familiar in the geological context, erosion-corrosion is a process which may have both mechanical and electrochemical aspects. In fact, even if the mechanical part of the process is negligible, as it often is at lower velocities, the enhanced corrosion due to flow is still called erosion-corrosion. The term erosion is sometimes used even more generally, to include the effects of direct liquid impingement and cavitation, but these processes are not normally found in simple flow over a plate or through a tube or channel. Thus the term erosion-corrosion is used typically in the literature in connection with any added increment of corrosion when a metal is exposed to a flowing electrolyte; in this case, the term is being related generally to any influence which velocity (in an undefined flow field) may have on the electrochemical/mechanical processes of erosion-corrosion.

We know that velocity can have a strong effect on corrosion rates. However, measurement of "velocity effects" is not as straightforward as it might seem, and there is a historical lack of correlation of corrosion rate data between various experimental studies, and the predictive value of the data to service situations is quantitatively unreliable. It will be shown in this paper that velocity effects for a given system are actually dependent on the local turbulence intensity; the higher the turbulence intensity, the higher the corrosion rate and the lower the critical value of the average velocity. This serves to point out that the average velocity is not a sufficiently descriptive factor to account for all the influences of a flow field on corrosion rate. It will be shown that more descriptive hydrodynamic parameters than the average velocity can be used to describe the effect of flow on corrosion rates. For the same average velocity, the flow structure can vary significantly due to such variables as tube diameter, surface roughness, protusions into a channel, bends, holes, etc. For example, boundary layer thickness and turbulence vary with tube diameter for the same velocity. Also, we know that turbulent flow and laminar flow have very different effects on corrosion, but it is not widely appreciated that for turbulent flow, which

predominates in service situations, the intensity of the turbulence is important, and is strongly affected by the particular physical situation. Because of these effects, it will be shown that disagreement among the results of corrosion studies involving velocity is not especially astonishing. It will be shown that only a model which includes the relevant hydrodynamic parameters can be expected to achieve consistency in the prediction of experimental results.

The purpose of the present research was to develop this philosophy in the study of velocity-affected corrosion. Experimentally, it was of interest to improve the experimental "circling foil" apparatus developed by Storm and co-workers (1) and to study various methods by which one can characterize the effect of "velocity" on corrosion rate of metals. It was of particular interest to experimentally determine certain fluid dynamics parameters, and to try to correlate non-dimensional parameters concerning hydrodynamics and diffusion with corrosion rate results. Also, it was of interest to study the corrosion morphology macroscopically and microscopically for different velocities (flow situations).

In the present experiments, CDA Alloy 706 (90/10 copper-nickel) was chosen as the sample material. Cu-Ni alloys are widely used in cooling systems containing corrosive liquids such as seawater. The flow velocity in these systems has to be limited, because it is recognized that while the corrosion rate is a weak function of velocity at lower velocities it increases drastically when a critical velocity is reached, the so-called breakaway velocity (2). For Cu-Ni alloys the breakaway velocity is in the range of 2 to 4 m/sec, a value which is seldom reached in normal pipe flow. The present experiments extended to 6 m/sec.

EXPERIMENTAL

The method chosen to deploy samples for velocity effects study involved moving the sample through a stationary body of fluid, i.e., the experiments were conducted in the opposite sense to those done in flow channels or other schemes where the fluid is moved past a stationary sample. In parallel work (3), studies were made on the same materials in a flow channel over the same nominal velocity range. The device used in the present work is literally a "circling-foil" apparatus. The apparatus originally designed by Storm and co-workers (1) was modified for the present experiments, with various problems inherent in the original apparatus overcome by design changes.

In the circling-foil apparatus, the samples are mounted flush in a streamlined plexiglas foil which circles in a horizontal plane within a tank (diameter about 1 m) of seawater (Figure 1). The path followed by the specimen in one revolution is 2 m long, so at 60 rpm (1 rps), a nominal relative velocity of 2 m/sec is obtained. The foil is deployed from a streamlined vertical strut which is connected in turn to the end of an arm which rotates in a horizontal plane above the fluid surface (see Figure 2). Therefore, only the foil and a portion of the vertical strut move through the fluid; the foil moves in a plane about 10 cm below the surface. This device is a relative to the rotating disc-plate type apparatus, which we have used in earlier studies (4), except that here we have a foil that represents just one small element of the disc plate. The primary advantages of this are: (1) there is far less force imparted to the body of fluid, and (2) there is not so large a radial component of flow developed over the surface for the same tangential velocity. Another aspect of this apparatus is that it requires much less plumbing than a flow channel system, and preserves the supply of electrolyte.

The samples are coin-like metal coupons mounted flush with the surface of the plastic foil, in closely fitted recesses (Figure 3). In earlier studies, we used square coupons mounted in metallographic resin; the present method allows easier removal and replacement. Samples can be deployed as single metal coupons or in galvanic couples. The individual recesses in the foil have external electrical connections to them, so that connections and electrochemical measurements can be made. For galvanic couples, a zero-resistance ammeter circuit is attached. Also, we can carry out linear polarization measurements during velocity runs, (see Figure 1) using one recess or the other as the working electrode, with the other as the counter electrode, or a stationary platinum disc positioned at the center of the tank can be used; a silver chloride reference electrode is also located at the center of the tank.

The foil has a profile designed to minimize wake (Figure 4). A trip wire is mounted on the nose to trigger turbulence in front of the specimen position. A stirring effect, which limited earlier work (1) to 3 m/sec, was substantially reduced by streamlining the vertical strut holding the foil, and concurrently stiffening it with an internal stainless steel tube. Also, additional anti-stirring baffles were added to the original tank (see Figure 5). These changes reduced the stirring velocity to a negligible value at the highest foil velocities used in this study (6 m/sec). The foil was connected to the strut at an angle of 9 degrees (see Figure 6) in order to ensure flow straight from

the front of the foil over the specimen, rather than diagonal. The specimens were 1.91 cm in diameter and 0.318 cm in height. The foil-to-specimen size ratio was a compromise intended to give low stirring and surface splashing, yet allow prediction of the flow features over the specimen position. The specimens were mounted in recesses machined with close tolerances, and hot paraffin was used to seal the specimen as it was pressed into the recess. The specimen could be easily pushed out of the seat through a hole in the foil after exposure. An ohmmeter was used before and after each run to check for good electrical contact between the specimen and the platinum-contact in the base of the recess.

The streamlined vertical strut contained a 0.48 cm O.D., 0.34 I.D. stainless steel reinforcing tube (Figure 3), and within this, two copper wires coming from the platinum contacts in the foil recesses; the strut-foil assembly was detachable from the horizontal support-arm via a BNC-connector. Transport of the signal from the electrodes in the foil to the external equipment was accomplished via a dual brass-slipring, phosphor bronze-brush arrangement at the top of the main shaft. This arrangement was quite successful, although electrical noise tended to increase with rpm. The top of the main shaft was fitted with a pulley wheel and 60-tooth gear (Figure 7). The latter was used to determine the speed of the foil via a magnetic sensor close to the gear which sent a signal at every tooth to a digital counter. Using the displayed Hz-number the speed could easily be determined. As the circumference of the circle described by the foil was exactly 2 meters, 1 RPS equalled 2 m/sec. The shaft was driven by a 1/4 Hp DC-motor via a pulley wheel-timing belt drive system, with transfer of the motor speed in a 1:4 step-down ratio. The motor was a Minarik Speed-control Model SH-63 ALI (Figure 7) with a maximum output of 3.5 amperes and maximum speed of about 1800 RPM, controllable to within about 1%.

The sample material was 90/10 copper-nickel (CDA Alloy 706). Samples were machined from 1.9 cm (0.75 in.) plate supplied by Anaconda Brass (specification given in Table I). The specimens were coin-like discs 1.9 cm diameter x 0.318 cm in height, surface prepared to 000 grit finish. After runs, specimens were cleaned with a soft brush and a solution of HCl, H₂SO₄ and water in the ratio of 5:1:4, as recommended by ASTM Standard G1-72, and the specimens were kept under vacuum until microscopic observations were made. For low magnification microscopic observations of the corroded

surfaces, a Bausch and Lomb Stereozoom Microscope was used (10X to 70X), whereas for higher magnifications (up to 400X) a Balplan reflected light conference microscope was used. In order to further increase magnification with high depth of field, a Cambridge S4-10 scanning electron microscope (SEM) was used, with which photomicrographs were obtained up to about 2000X.

The electrolyte was synthetic seawater prepared by standard methods (5). Temperature, pH, conductivity, and oxygen content of the electrolyte were monitored during and after the corrosion tests. Temperature was $20^{\circ}\text{C} \pm 0.15$, pH was 7.85 ± 0.15 , and specific conductance was $4 \times 10^4 \pm 0.15 \mu\text{hos/cm}$. At the higher velocities, the solution tended to increase in temperature by several degrees over the course of a 24 hour run.

Four nominal test velocities were used: zero velocity, 2 m/sec, 4 m/sec, and 6 m/sec. Several different methods were applied to determine corrosion rates, including weight loss (WL), linear polarization method (LPM), galvanic current (ZRA), and potentiodynamic polarization curves (PPC). Specimens were tested as single metal coupons and as members of galvanic couples with platinum cathodes. Table II summarizes the experimental matrix that was conducted.

Weight change measurements were converted to corrosion rates in mdd ($\text{mg}/\text{dm}^2\text{ day}$), mpy (mils per year, i.e., 0.001 inches per year), and μmpy (10^{-6} meters per year) by the relations:

$$R_{\text{mdd}} = \frac{WL}{At} (2.4 \times 10^3)$$

$$R_{\text{mpy}} = \frac{WL}{At_p} (3.45 \times 10^3) \quad WL \text{ (mg)}$$

$$= R_{\text{mdd}} \left(\frac{1}{\rho} \right) (1.44) \quad A \text{ (cm}^2\text{)}$$

$$R_{\mu\text{mpy}} = \frac{WL}{At_p} (87.6 \times 10^3) \quad t \text{ (hours)}$$

$$= R_{\text{mpy}} (25.4) \quad \rho \text{ (g/cm}^3\text{)}$$

LPM measurements of $\Delta I/\Delta E$ (Fig. 8) were converted to corrosion current through the Stern-Geary relationship, using the equation:

$$i_{\text{corr}} = 0.026 \Delta i/\Delta E \quad i_{\text{corr}} \text{ (\mu A/cm}^2\text{)}$$

$$\Delta i \text{ (\mu A/cm}^2\text{)}$$

$$\Delta E \text{ (volts)}$$

Corrosion current density, i_{corr} , obtained from LPM or PPC, or i_{couple} , obtained from ZRA, can be converted to corrosion rate according to the relation:

$$R_{md} = \frac{i_{corr} (A/Z)}{F} (8.6 \times 10^3)$$

i_{corr} ($\mu\text{A}/\text{cm}^2$)
 A/Z (g/equiv)
 F (96,500 A-sec/equiv)

$$= i_{corr} (A/Z) (8.9 \times 10^{-2})$$

The corresponding penetration rate can be obtained from

$$R_{mpy} = \frac{i_{corr}(A/Z)}{p} (0.13)$$

The effective equivalent weight, A/Z, for the 90/10 copper-nickel alloy was calculated from simple rule of mixtures relations, using the expressions:

$$\bar{A} = A_{Cu} X_{Cu} + A_{Ni} X_{Ni}, \text{ where } X = \text{mole fraction}$$

$$\bar{Z} = Z_{Cu} X_{Cu} + Z_{Ni} X_{Ni}.$$

It was assumed that $Z_{Cu} = 1$, based on conversion to cuprous oxide (Cu_2O) and $Z_{Ni} = 2$, based on conversion to nickel oxide (NiO).

The mole fractions were calculated as follows:

$$X_a = \frac{C_a}{A_a} \cdot \frac{1}{\text{total moles}}$$

$$\text{and total moles} = \frac{C_a}{A_a} + \frac{C_b}{A_b}, \quad C = \text{weight percent in alloy.}$$

The result for 90/10 copper-nickel is $A/Z = 56.6$ g/equiv.

Linear Polarization Method (LPM): LPM measurements were used to determine the corrosion rate as a function of time and velocity. These data were then compared to those obtained from direct weight loss measurements and from other methods. The equipment for the LPM measurements consisted of a Princeton Applied Research potentiostat-galvanostat, Model 173, and Universal Programmer, Model 175, and a Hewlett-Packard Model 7040A recorder (see Figure 9). Independent LPM data were gathered at zero velocity using a standard

laboratory corrosion cell and the circling foil tank. The standard laboratory cell employed a silver-silver chloride reference electrode and two carbon rods as the counter electrodes, whereas for tests in the circling foil tank, the counter electrode was a platinum plate, placed at the center of the bottom of the tank to maintain the same distance to the rotating foil at all times. In several tests a platinum counter electrode was placed together with the working electrode in the foil recesses, with no apparent difference noticed in the measurements. Thus the usual procedure was to use the two recesses in the foil for a pair of copper-nickel samples, with the specimen used subsequently for weight loss determination, and the other for macroscopic and microscopic examination of the corrosion of the exposed surface.

Calculations of corrosion current from the LPM measurements were based on the standard Stern-Geary expression:

$$\text{Polarization Resistance} = \Delta E / \Delta I = \frac{\beta_a \cdot \beta_c}{2.3 I_{\text{corr}} (\beta_a + \beta_c)}$$

Rearranged, this becomes:

$$I_{\text{corr}} = \frac{\beta_a \cdot \beta_c}{2.3 (\beta_a + \beta_c)} \cdot \frac{\Delta I}{\Delta E}$$

where β_a and β_c are the anodic and cathodic Tafel slopes, respectively, and $\beta_a \cdot \beta_c / 2.3 (\beta_a + \beta_c)$ is a constant, k.

Stern and Geary (6) determined the value of the constant by assuming a theoretical value of 0.12 volts for the Tafel slopes. Pye (7) also calculated k for various materials and came to the same result, i.e., $k = 0.026$, so that the final formula for the corrosion current density reads:

$$i_{\text{corr}} = 0.026 I_{\text{appl}} / \Delta E \cdot \text{Area}$$

for area in cm^2 , i_{corr} in $\mu\text{A}/\text{cm}^2$. This equation was applied to calculate corrosion rates from LPM measurements in this study. The value of k determined in this study from potentiodynamic polarization curves was 0.024, which is very close to the theoretical value for copper.

The LPM method provides a rapid measurement of relative corrosion rates or changes in corrosion rates; but the accuracy of the absolute value of the corrosion rate determined from LPM is of concern to many electrochemists (6,7);

benerally the corrosion rate determined by LPM is with in a factor of two or three of the actual corrosion rate. The advantages of LPM are that this method is not nearly as tedious, difficult or time-consuming as conventional weight loss determinations, and it can be applied to electrodes which are very difficult to reach, for example in pipes. Also because of the possibility of measuring small corrosion rates and the transient behavior of the corrosion, this method is of value.

In a recent report by Macdonald, Syrett and Wing (8) the LPM method and other polarization resistance methods, such as the AC impedance method and the potential step method, were used to study corrosion in flowing seawater and the agreement of the three methods with weight loss determinations was very good. These authors point out that the LPM-method is quite reliable if correctly applied, but two problems concerning the LPM-method are emphasized. First, any electrochemical reaction, whether it leads to corrosion or not, will contribute to the current; for example, hydrogen oxidation can give rise to an anodic current which is not distinguishable or separable from the corrosion current when measured by the LPM-method. The other problem refers to the polarization resistance, $R_p = dE/dI$, which, as experimentally determined, actually is the impedance of the interface, containing capacitive and inductive components in addition to the ohmic resistance when time dependent signals are involved. Only at low frequencies are the capacitive and inductive parts negligibly small. Thus slow scan rates will help to avoid this problem. In these experiments a scan-rate of 1mV/sec was applied, over a range of $\pm 10\text{mV}$, in order to minimize the problem mentioned above.

The first LPM measurements were made 2 minutes after the velocity started and the frequency of the measurements decreased with increasing time (Figures 16, 17, 18, to be discussed later). In order to increase the readability of the slope on the plots, the sensitivity of the current axis was adjusted to give a slope of about 45° . At this sensitivity, some noise from the stop ring contacts was detected, but one could still read the current corrently within about $\pm 3\mu\text{A}$. Thus, the uncertainty became about 10%, because the absolute value of I ranged from 25 to 50 μA . The IR drop in the seawater electrolyte was considered negligible compared to the polarization resistance and was neglected. To reflect the change in corrosion rate with time, the individual points obtained by the LPM method were plotted versus time, and to compare these results with

corrosion rates determined by other methods, an average value of i_{c} was determined graphically.

Potentiodynamic Polarization Curves (PPC): Potentiodynamic polarization curves were obtained at various velocities. The potentiodynamic polarization method is essentially similar to the LPM method concerning the equipment used, and as the method itself is widely known, a detailed description will not be given here. This technique is usually performed with the standard corrosion cell, but in order to support and compare the corrosion data gained by other methods in this research, polarization plots were also obtained for specimens in the circling foil tank at different velocities.

Although only small currents are involved in the polarization measurements the results were good considering the speed and the noise (Figs. 20-22). Since the polarization plots are basically developed in the same way as the LPM-plots, one might expect similar noise problems. But the sensitivity to noise was much less, because of the greater range of current: 100 mA on these plots, and $\pm 30 \mu\text{A}$ on the LPM plots. In general, the other problems described in the last section applied to the polarization curves as well. In order to detect flaws in the set-up, several test runs were performed with a standard flask. No significant difference could be observed, and repetitions of runs showed good reproducibility.

Zero-Resistance Ammeter (ZRA): The design of the foil (see Figure 4) allowed tests involving natural galvanic couples. Because the corrosion rate of the copper-nickel alloy is quite low, some experiments were designed to accelerate the rate by using a galvanic couple of the copper-nickel alloy with platinum cathodes. Furthermore, galvanic coupling made it possible to measure the corrosion rate as a function of time and velocity by using a zero-resistance ammeter (ZRA) (9,10). A schematic drawing of the ZRA is shown in Figure 10. In the arrangement actually used in these tests the working electrode (WE) was a copper-nickel specimen, the counter electrode (CE) was a platinum disc positioned stationary at the center of the tank, and the reference electrode (RE) was silver-silver chloride, also positioned at the tank center. The two ZRA output voltages E_0 and V_0 (see Figure 10) were measured by two digital voltmeters (Weston, Model 1240 and Model 4444) and recorded versus time by a stripchart recorder (Moseley Autograf Model 7100 BX) (Figure 11).

Hot film Anemometry: Since one purpose of this study was to find a correlation between corrosion rate and hydrodynamic variables, efforts were made to determine some of these variables. The simplest flow parameter to obtain is the relative velocity of the sample with respect to the fluid. This can be measured with a calibrated anemometer or, if one neglects any possible rotational velocity of the body of electrolyte, the relative velocity can be calculated directly from the RPM of the main shaft. The dimensionless Reynolds number, Re , can be calculated from the flow velocity and fluid properties. The Schmidt number is also determined without any experiments, from the viscosity and diffusion coefficient. A variable which can be obtained only by direct measurements is the turbulence intensity, defined as the ratio of the rms fluctuation in velocity and the mean velocity (U'/\bar{U}). In the present work, only velocity fluctuations in the direction of net flow (horizontal or x-direction) were determined; the vertical component, which may also be important in the erosion-corrosion process, was not measured. The turbulence intensity was calculated from the relation (11, 12):

$$\frac{U'}{\bar{U}} = \frac{4 e' V}{V^2 - V_0^2}$$

where

e' = rms voltage fluctuation (turbulence), read on an RMS-voltmeter (volts)

V = bridge voltage, read on digital-voltmeter (volts)

V_0 = voltage at zero velocity (volts).

In order to measure the unknown quantities in this equation (e' , V , V_0) the following equipment was used (Figure 12): TSI Model 1050 constant temperature anemometer, TSI Model 1050-1D monitor and power supply, and TSI Model 1060 RMS voltmeter. Two types of hot film probes were used: TSI Model 1231 conical probe, and TSI Model 1261 miniature boundary layer probe. Probe 1231 is a widely-used, rugged sensor that inhibits contamination and resists breakage, but with limited sensitivity due to its shape, the size of the cone, and the position of the sensor tip, which does not allow measurements closer than 1 mm to the surface; also, it is difficult to determine the exact

distance to the surface. The 126i probe is designed to measure velocity and turbulence as close as 0.1 mm to the surface, in order to determine the hydrodynamic boundary layer. However, this probe is very sensitive to contamination and mechanical load. Figure 13 shows the design to hold the probe above the surface of the foil. Thin plates of a known thickness put under the protecting pin can be used to determine the exact distance to the wall, which is 0.125 mm without any plate.

All unknowns in the turbulence intensity equation shown above can be read directly from the instruments described. The voltage at zero velocity, V_0 , is obtained by extrapolation of a plot of e^2 versus the square root of the apparent velocity (Fig. 14). The apparent relative velocity U is calculated from the RPM and e is the voltage given on the digital meter. V_0^2 is the intersection of the extrapolated line of e^2 versus the square root of U with the e^2 axis. The value of V_0 could be approximated by measuring e at zero velocity directly, but one has to be aware of the possible error due to the influence of free convection at zero velocity, whereas it is negligible at higher velocities.

Anemometric measurements of this sort are subject to some problems. First, the boundary layer probes are sensitive to mechanical wear and prone to failure by this mode. More durable probes tend to be less sensitive. In our measurements, a compromise was made; turbulence intensity was not measured at distances from the wall closer than 1 mm, and the sensitivity was probably not sufficient to completely detect the size of the eddies of the turbulence structure. Therefore the results must be regarded as incompletely descriptive of the flow structure. In the present case, another difficulty in determining the turbulence intensity with hot film probes was the existence of a general wake-induced structure due to the motion of the foil-strut assembly through the tank. Because of the relatively small size of the tank the foil continuously ran through its own wake, creating a complex flow structure on the tank, with the effect more pronounced at higher velocity. In this situation, the probe must also detect the general turbulence structure set up in the tank, as well as the turbulence intensity directly caused by the motion of the plate through the fluid. If this background noise is high, the signal due to the true flow structure over the foil will be masked. In such case, a spectrum analysis can help to determine the size and energy of the eddies; such analyses were not undertaken in the present study.

The turbulence measurements (Table III) indicate rather high values, even at large distances from the foil, reflecting the large-scale flow structure set up in the tank at higher velocities. The 15 mm value was taken as the free stream turbulence intensity; the values of 3% - 6% are rather high but not unreasonable. Considering this high free stream turbulence intensity, the results of 25-30% for the turbulence intensity close to the foil also seems not to be unreasonable. The relative velocity determinations indicated by the bridge voltage never dropped considerably as the foil was approached by the probes, so that it must be assumed that the probes were not brought inside the boundary layer.

RESULTS

1. Effects of Velocity on Corrosion Rates

In this section the corrosion rates determined by weight loss, LPM, and other methods will be compared for various velocities. Table IV summarizes the results for 2 m/sec, 4 m/sec and 6 m/sec.

WL and LPM: The LPM results are presented in Figures 15-19. At a velocity of 2 m/sec the corrosion rates determined by WL and LPM were approximately equal at about $9.5 \mu\text{A}/\text{cm}^2$, which is about 40% higher than the rate given in the literature for 1.6 m/sec (8). It is interesting to note the lower corrosion rate determined by the LPM method when taking measurements from a sample immediately after it had been disconnected from a galvanic couple. Although the corrosion rate of the coupled specimen is higher than that of a single metal specimen, the coupling has the opposite effect on the LPM corrosion rate results for the specimen when disconnected. During the time the LPM measurement is being performed, the couple was disconnected and the single metal polarization resistance corrosion determined. Since the surface is already heavily corroded due to the galvanic action, a thicker barrier has built up and the single metal corrosion rate is therefore decreased. This effect was observed at all velocities, so that these (disconnected galvanic couple) data were not used for a direct comparison of the effect of velocity on corrosion rates. The ZRA data on these coupled samples will be discussed later.

An increase in velocity to 4 m/sec did not result in a large increase in corrosion rate. The LPM determinations for this velocity show a slight increase,

but weight loss measurements (Runs 7, 15) show no substantial increase. Again, a lower rate is observed for disconnected galvanic couples (Run 3).

At 6 m/sec, a more substantial increase of corrosion rate is seen. Except for results from decoupled specimens (e.g., Run 5), the rate increased noticeably, from 12 to 14 $\mu\text{A}/\text{cm}^2$ (LPM) and from 10 to 12 $\mu\text{A}/\text{cm}^2$ (calculated from weight loss) relative to 4 m/sec. Runs 16 and 18 at 6 m/sec exhibit a peculiar behavior not observed at other velocities: the rate in both runs decreased with time from a high initial point, as expected, but did not maintain a low rate plateau as for other runs; rather, the rate increased again after 5 or 6 hours, then decreased again after several hours. The explanation for this deviation from steady state behavior may relate to the effects of higher velocity on the surface structure. After a certain corrosion layer has built up, the rate may decrease due to the greater barrier, but under the continuing action of the flow structure, e.g., due to high local stresses associated with the amplified action of energetic eddies (note the high turbulence intensity), perhaps in combination with the action of entrained bubbles, the layer may be effectively "worn" thin, so that the corrosion rate may increase again. This action may be cyclic in nature.

Another possible effect could be due to temperature, which increased during the first several hours of 6 m/sec runs (from 20°C to 24°C); constant afterwards. This temperature increase was only seen at 6 m/sec. It is generally the case that an increase in temperature accelerates corrosion. Further research to study the temperature/velocity interaction may be in order. However, the fluctuation in polarization resistance with time at 6 m/sec was seen for several different experimental runs, while temperature was constant, so that the existence of some sort of time-dependent phenomena is certain. Plots of i_{couple} vs. time from ZRA exhibited a slow and continuous decrease with time at 6 m/sec.

Polarization Curves: In principle, the corrosion current density can be obtained by the intersection of the Tafel slopes of the anodic and/or cathodic branches of the polarization curve with the corrosion potential. However, the successful application of this method in practice requires curves with reasonable well-defined Tafel regions, the slopes of which can easily be determined. The actual plots, however, did not show this nice feature (Figs. 20-22), and determination of corrosion rates via the Tafel slopes shows some inconsistencies for this reason. The results show good correlation with WL and LPM for most velocities. The result for 2 m/sec cannot be regarded as reliable.

(the value of $i_c = 21 \mu\text{A}/\text{cm}^2$ is more than double that obtained by the weight loss and LPM methods), because the slopes of the polarization plot are difficult to measure exactly. The results for 4 m/sec and 6 m/sec are $14 \mu\text{A}/\text{cm}^2$ and $16 \mu\text{A}/\text{cm}^2$ respectively. They are also above the other measurements, but only by about 25%. The general trend is an increase of corrosion rate with velocity, and a decrease in the corrosion potential.

ZRA: The ZRA galvanic current results are important relative to the time-dependent behavior of couples. The results will be compared with the weight loss and other results. Some of the ZRA results are given in Figure 23. All results of tests involving couples were comparable to those determined by weight loss. The transient ZRA curves for corrosion rate shown in Figure 24 showed generally the same trend as did LPM measurements (Figures 16-18). Starting from a fairly high initial value the corrosion rates dropped until, after 5-6 hours, a plateau value was obtained, with a gradual decrease in corrosion rate along this plateau. The corrosion rate had not stopped decreasing after 24 hours. This effect is not so obvious in the plots shown in this paper because of the compressed axis. Probably due to the less continuous method of measurement, the LPM curves do not reflect this slow decrease (Figs. 16-18). Both the ZRA and LPM curves describe a parabolic shape, which Popplewell (13) has suggested is typical for Cu-Ni alloys. The decrease in corrosion rate is related to formation of a barrier oxide film as time goes on. All the transient curves of corrosion rate show about the same time spent to reach the plateau condition (stable corrosion rate), but there is a marked difference in the magnitude of the rate (after 24 hours) for different velocities.

2. Corrosion Products and Surface Morphology

In an attempt to identify corrosion products, the surface of the most heavily corroded samples (in terms of surface product) were exposed in the x-ray diffractometer. However, the corrosion product accumulations were either too thin or the size of the corrosion product particles was too small to give a coherent diffraction pattern; the only pattern detected was that of the base metal. Also, X-ray fluorescence spectroscopy using the Scanning Electron Microscope in connection with a computerized X-ray analyzer (PGT 1000) did not give any additional information. Some constituents other than those of the base metal could be detected, but the reliability of the determination was low because of lack of resolution.

Light microscopy was used to compare the colors of the products with the known colors of possible corrosion products. By the naked eye, the surfaces generally seemed to be covered with a dark, dull-looking layer, but in the light microscope, a green color was seen, ranging in shade from light to dark. Imbedded in the green colored film were singular red spots and in some small areas the bronze color of the base metal shined through. The variation in the shade of green was probably due to varying thickness of the layer; the thicker it was, the darker the color. This also probably gave rise to the macroscopic blackish appearance of the surface. At high magnification one could observe very dark coloration along lines of preferential corrosion.

Comparing these colors with those given by the Handbook for Chemistry and Physics (14) one has the selection of possible corrosion products shown in Table V. There are many more possibilities, of course, because of the variety of constituents in the seawater. But considering the major products reported in the literature, the oxides and chlorides are the most likely corrosion products.

Macdonald and co-workers (8) mention in a recent report that the corrosion potentials ranging from about -0.05 to 0.15 V with respect to the Standard Hydrogen Electrode (SHE) in a solution with a pH-value of 8 lie in the stability region for the cuprous oxide, Cu_2O , but also close to the equilibrium potentials for $Cu_2(OH)_3Cl_2Cu_2O$. These results are taken from the pH/potential diagram given by Bianchi and Longhi (15). They also mention the existence of a thin green layer on the surface. Since these stated conditions are similar to those in the present study, one may assume similar corrosion products. Cu_2O is red and copper hydroxychloride is green, and these are the dominant colors of the corrosion products on these specimens. However, this does not explain the blackish appearance which the surface presents to the naked eye.

A possible reason for the dark color could be copper sulfide (CuS), although it would not be expected unless the synthetic seawater solution somehow had become contaminated with sulfur or sulfides. A test described by Feigl(16) was performed by putting a drop of sodium azide and potassium iodide solution together with a bit of the corrosion product. If at once a vigorous reaction starts, with rising bubbles (sulfide acts as a catalyst for nitrogen evolution), sulfide is one of the corrosion products. Using mechanically removed solid corrosion products combined with a platinum wire (as described by Feigl), the test showed no reaction. The electrolyte in the tank

was tested in the same way, with no sign of sulfide, although this method is supposed to detect sulfide at very low concentration. The conclusion is that there is no evidence of any sulfide contamination.

The morphology of corrosion products, in galvanic couples of 90/10 copper-nickel alloy and platinum, after exposure of 2¹/2 hours, consists of a considerable layer of corrosion product on the surface. Figure 24a shows an as-exposed surface (not cleaned after exposure). Streaks in several directions are seen. The flow (left to right) had an obvious effect on the pattern of the corrosion layer (although the set of lines parallel to the flow were not caused by the flow, but are simply the grinding marks running parallel to the flow). On the other hand, the sets of streaks at angles to the flow direction may have originated in the flow pattern over the surface. They look similar to the fine undulating surface topology often found in sandy ocean bottoms. But whereas those patterns are typically rather uniform, the corroded surfaces of these specimens exhibit an irregular pattern, probably related to the irregular flow over the plate, including such features as side flow effects from the edges of the foil. All specimens tested as couples showed a similar formation of corrosion products. One can see macroscopically that the corrosion layer appears flat black, and is irregular in thickness (in the streaked pattern). Figure 25 shows closer views of these variations in thickness in photographs made with a standard light microscope.

In Figure 24b a SEM-photo shows the surface as-corroded when run at a velocity of 6 m/sec. The white flecks on the surface appear dark in the light microscope. One can see the grain boundaries of the base metal and sets of fine lines which have different directions in different grains, and which appear to be local crystallographic lines of dissolution. These fine lines probably correspond to those shown in Figure 26 on a polished and etched surface; they are sets of slip lines in the cold-worked grains.

Although still covered with corrosion products, the surface in Figure 24c illustrates the regular fine-scale pitting nature of the dissolution morphology. The corresponding cleaned surface (Fig. 27) offers a clearer view of these dissolution surfaces. In Figure 27a one can see some boundaries and observe preferential attack along grinding marks; Figure 27b shows the character and scale of the pitted surface. The individual pits are about 2-3 μm in diameter and very densely spread over the whole surface. In the light microscope (Figure 28), the cleaned surface of a coupled specimen shows a

similar etched appearance as the metallographically prepared sample in Figure 26. But the specimen corroded in seawater (Figure 28) shows many short curly lines of attack, with a length of about 20 μm . It is not clear whether these lines have anything to do with the flow over the specimen. These lines probably do not correspond to small eddies, as one might expect from their shape, because they are smaller than the scale of such eddies in the flow structure.

In single metal exposures of up to 48 hours, the corrosive attack was much less than for coupled specimens, as one could expect. Because of the lower amount of corrosion products, the wave-like pattern seen on the coupled specimens was generally not detected; only specimens exposed at 6 m/sec showed the beginning of such a pattern. For single metal exposures, the surface was typically covered much more evenly by a blackish corrosion product layer, with a slight purplish sheen.

At 100X, the as-exposed surface exhibits no special features (Figure 29a). The only difference from the initial surface is that the grinding marks are not as distinguishable as before corrosion. Figure 29b shows preferential attack on the grinding marks, but no special feature which could be related to the effect of velocity. Figures 30a and 30b, however, are good examples of accelerated corrosion at higher velocities. At higher magnification, the cleaned surfaces show preferential attack on the grinding marks and a few individual pits distributed over the surface; relative to the coupled specimen (Figure 27) the pit structure is much less uniform.

There is a distinct difference in corrosive attack as a function of velocity. For example, in Figure 30, for 2 m/sec and 6 m/sec, it is seen that the specimen exposed at 6 m/sec has corroded much more than the one exposed at 2 m/sec. Whereas the corrosion of the latter specimen took place for the most part at the grinding marks, the attack of the specimen exposed to the higher velocity seems to have occurred uniformly but not less intensely, over the whole surface; the entire upper layer of the 6 m/sec sample has been corroded away. The same behavior is illustrated in Figure 31 at lower magnification; also, one may notice an increase in the number of dissolution sites (pits) as velocity increases.

Limited tests in static conditions were performed. After an exposure of three days without aeration (which means that the oxygen content of the solution was much less than in a dynamic exposure) the specimens showed a different surface than for dynamic exposures. The dominant colors were green and red;

the surfaces were very shiny, but the corrosion product films were not nearly as dense as in the dynamic tests. At some spots a darker brownish layer could be detected, but the blackish coloration of the dynamic tests is not seen. Figure 32 shows an example of the surface of a statically exposed specimen. In general, attack was visibly much less severe than on specimens subject to dynamic exposures.

The fairly rough and non-uniform attack seen on micrographs taken with the SEM is probably caused by precipitated copper hydroxychloride, because the possible oxides more typically form fairly uniform thin films, as pointed out by Blundy and Pryor (17); both Cu₂O and NiO would tend to form such films.

DISCUSSION: HYDRODYNAMIC CONSIDERATIONS IN CORROSION

1. Boundary Layers in Turbulent Flow

Basically there exist two flow regimes: laminar and turbulent. This study and that of Schack (3), performed concurrently at NPS, involved for the most part turbulent flow, so discussion of the boundary layer system in this chapter emphasizes turbulent flow. While this study used a moving foil as the specimen holder, Schack used a water channel with the sample built flush into one side. However, the flow system over the foil can be approximated by the flow over a flat plate, for which the hydrodynamic analysis is well-known.

The boundary-layer thickness is generally defined as the distance from the "wall" to the point where the velocity becomes equal to 99% of the free stream velocity. Since this boundary layer is dependent only on hydrodynamics, it is called the hydrodynamic boundary layer (d_h). Most of the other boundary-layers are in one way or the other related to the hydrodynamic boundary-layer. Figure 33 shows the boundary-layers which must be considered relative to the erosion-corrosion process. This configuration approximates the well-known Levich theory (18) except that Levich did not have a buffer zone in his model.

Above a critical velocity (in a system where all other variables are kept constant), the flow over a flat plate changes from laminar to turbulent in character. This does not occur suddenly, but within a range called the transition range. The range in which transition from laminar to turbulent flow occurs can be determined by using a non-dimensional flow-parameter, the Reynolds number, Re , defined as $Re_x = Ux/v$, where U is the free stream velocity (m/sec), x is the characteristic length along the plate (m), and v is the kinematic viscosity (m^2/sec). Transition may occur at a Reynolds number between 10^5 and 10^6 in the case of a flat plate, depending on other factors such as free-stream turbulence intensity, surface roughness, pressure gradients (due to the shape of the body), and protrusions from the surface, which tend to trigger ("trip") turbulence. Tripping was applied in the present study to ensure turbulent flow over the specimens. The tripping, the high free stream turbulence intensity and the flow velocity gave rise to high intensity turbulent flow over the specimens. In the concurrent flow channel

experiments (3), the turbulence arose due only to the characteristic length and the flow velocity, and tended to be lower for the same nominal relative velocity.

The turbulent boundary layer grows in thickness much more rapidly along the streamwise direction than does the laminar boundary layer. Also, due to the turbulent mixing, the shear stress in turbulent flow is greater than in laminar flow at the same boundary-layer thickness. Because of the random motion of the fluid particles in turbulent flow it is more difficult to model the flow parameters theoretically and it is also more difficult to measure them. In spite of these problems formulae for the hydrodynamic layer and viscous sub-layer are well established. Schlichting (19) mentions the following relations:

$$(1) \quad d_h = 0.384 \times Re_x^{-0.2}$$

$$(2) \quad d_{sl} = 71.4 \times Re_x^{-0.9} .$$

The laminar sublayer, d_{sl} , also called the viscous sublayer, is a region where the velocity has decreased to such an extent that the viscous forces dominate over the inertia forces; the flow is not considered to be perfectly laminar, so the term laminar sublayer is misleading. Between the laminar sublayer and the fully turbulent region there is a transition region called a buffer zone, where both the viscous and inertial forces are important, whereas in the outer, fully turbulent region the inertial forces dominate.

An important boundary layer relative to electrochemical processes is the diffusion boundary-layer, δ_d . The diffusion boundary-layer relates to the mass-transfer of species from the electrolyte to the corroding surface, or from the surface to the electrolyte; therefore this layer is also often called the mass-transfer boundary-layer. Unfortunately, there exist only a few literature sources which describe the actual thickness of this boundary-layer over a flat plate under hydrodynamic conditions.

The dimensionless Schmidt-number has been used to relate d_d to the thickness of the hydrodynamic boundary-layer d_h by the formula:

$$(3) \quad Sc^{1/3} = d_h/d_d$$

which is comparable with the relation in heat transfer:

$$(4) \quad Pr^{1/3} = d_h/d_T ,$$

where d_T is the thickness of the thermal diffusion boundary layer and Pr is the Prandtl number. The Schmidt number is fundamentally defined as:

$$(5) \quad Sc = v/D$$

where

v = kinematic viscosity (m^2/sec)

D = diffusion coefficient (m^2/sec).

The Prandtl-number in heat transfer is a similar dimensionless parameter, defined as:

$$(6) \quad Pr = v/\alpha$$

where

α = thermal diffusivity (m^2/sec).

Wranglen and Nilson (20) calculated d_d for laminar and turbulent flow. For laminar flow, they assumed that the velocity profile as given by Eckert (21) is equal to the concentration profile and by using the relevant boundary layer mass-transfer equations they determined d_d for a system with an initial length; i.e., the corroding specimen (as in the present experiments) is positioned a certain distance from the leading edge, a distance over which no diffusion is possible. Their result was:

$$(7) \quad d_d = 4.53 \times Sc^{-1/3} Re_x^{-0.5} [1 - (x_0/x)^{0.75}]^{1/3}$$

where

x_0 = initial length.

For x_0 equal to zero, it is possible to show that the relation $Sc^{1/3} = d_h/d_d$ is valid for laminar flow. For laminar flow $d_h = 4.53 \times Re_x^{-0.5}$ (35). Using this relation for d_h in the ratio d_h/d_d one gets $Sc^{1/3} = d_h/d_d$.

However, for turbulent flow, the equation given by Wranglen for the diffusion boundary layer does not allow a simple relation between Schmidt-number and the thickness of the turbulent diffusion boundary layer. Assuming a linear concentration profile d_d can be determined as follows:

$$(8) \quad d_d = 6.9 \times Sc^{-1/3} Re_x^{-0.6} \cdot [1 - (x_0/x)^{0.9}]^{1/3}.$$

Combining this equation with the equation of d_h in turbulent flow, one obtains

$$(9) \quad d_d/d_h = (17.9 Re_x^{-0.4}) Sc^{-1/3}$$

where it is obvious that $Sc^{-1/3}$ is not equal to the ratio of d_h and d_d , but only proportional to it with a proportionality factor of $17.9 Re_x^{-0.4}$. This factor is smaller than unity for Reynolds number greater than 1500, so that d_d determined by this equation is smaller than that given simply by $Sc^{1/3} = \delta_h/\delta_d$, to a degree which depends on the Reynolds number.

Figures 34 and 35 show the evolution of the various boundary layers with distance over a flat plate, according to the various formulae. It can be seen that the development of δ_d according to the simple relation $\delta_d = Sc^{-1/3} \delta_h$ predicts that δ_d soon becomes thicker than the viscous sublayer. But the nature of the viscous sublayer demands that the diffusion boundary layer is normally smaller than the viscous layer. Levich (18) states that the diffusion boundary layer in turbulent flow is less than the viscous sublayer and that turbulent mixing ensures a constant concentration throughout the entire hydrodynamic layer and in the outer zone of the viscous sublayer. Also Ross (22) indicates that d_d in turbulent flow is less than d_d under the streamline conditions of laminar flow. However, this would not be the case if the relation $d_h/d_d = Sc^{1/3}$ is valid for turbulent flow, because d_h (turbulent) is greater than d_h (laminar). Ross also accepts the equations for d_d (turbulent) of Wranglen.

The well established fact that the diffusion rate is higher in turbulent flow than in the streamline conditions of laminar flow at the same characteristic length gives a further reason for the assumption that the Schmidt number is not a valid measure for d_d in turbulent flow. Higher diffusion rate demands a smaller diffusion boundary layer, but d_d in turbulent flow would be greater than d_d in laminar flow using the Schmidt number, because d_h (turbulent) is greater than d_h (laminar). Some literature sources do suggest that the exponent of the Schmidt number when using the ratio d_d/d_h varies depending on the flow regime; however, there is no information in the literature on exactly how the exponent varies with velocity or Reynolds number.

An additional feature of the Wranglen equation is the initial (no-diffusion) length which is included to account for the general case. This feature is

very important, because (at least in laminar flow) the ratio of d_h and d_d is constant only if both layers commence at the leading edge. As pointed out in the literature, if d_d starts at the leading edge, it grows fast in the beginning phase, and levels off at a greater distance x from the leading edge. Comparing the two relations for d_d plotted in Figure 35 it is easily verified that only the Wranglen equation has this feature. Further, according to equation (8) derived earlier, the higher the velocity, the greater the Reynolds number and the smaller is the diffusion boundary layer, which encourages faster diffusive transport of oxygen to the metal surface, resulting in a higher corrosion rate.

2. Mass Transfer Considerations

Corrosion in electrolytes can be described by fundamental electrochemical reactions. The following mechanisms are important: (1) transport of certain species to and from the surface, (2) reaction at the metal/solution boundary, and (3) removal of the corrosion products.

The mechanism by which ions arrive at and leave the corroding surface can be generally described as diffusion, although one must distinguish between different types of diffusion. The classical formula for mass transport (Fick's First Law) is given by:

$$(9) \quad j = D \Delta c / d_d$$

where

j = mass transported to the surface ($\text{mol}/\text{cm}^2\text{-sec}$)

D = Diffusion coefficient (m^2/sec)

Δc = Concentration difference between electrolyte and surface (mol/m^2)

d_d = effective diffusion boundary layer thickness (m)

As can be seen from this formula, a decrease in d_d results in an increase in the mass transport flux, j , and this corresponds to an increase in the corrosion rate.

In a completely calm electrolyte, molecular diffusion due to concentration differences is the dominant mechanism. Because the diffusion coefficient in fluids is rather low, the reaction rate in such an electrolyte is relatively low. But when species are transported by convective flow

in addition to the molecular diffusion mechanism, the net flux at the surface increases considerably. Transport by convective motion is called "convective diffusion". Convection itself may be separated into free and forced convection. At any reasonable velocity the latter is dominant; only for static conditions or at very low velocity does free convection play a significant role.

A term may be added to the standard diffusion equation (Fick's First Law) to account for the additional diffusion due to turbulence, by the introduction of a turbulence diffusion (eddy diffusion) coefficient ϵ (22), so that:

$$(10) \quad j = (D + \epsilon) c/d_d$$

This corresponds to the relation given by Holman (23) in heat transfer.

The mass transfer equation reveals that an increase of the diffusion coefficient D results in an increase in the mass transfer rate, j . However, increasing D causes a greater diffusion boundary layer thickness d_d (equation (8)), and as seen in equation (1) and as mentioned often in the literature; larger d_d results in a lower mass transfer rate, because the concentration gradient is not as steep. This contradiction can be cleared by recognizing that d_d changes only as the $1/3$ power of D , so that the direct effect of increasing D is only partly diminished through its effect on d_d . Thus an increase in D dominates the situation, giving a net increase in mass transfer. Conversely, if a decrease in d_d is caused by a decrease in diffusion coefficient only, the general rule (as stated often in the literature) that a decrease in d_d tends to accelerate the mass transfer rate is not valid, because the decrease in D which leads to lower d_d dominates the situation, resulting in a net decrease in mass transfer (see equation (9)). The general rule is only applicable when the change of d_d is not caused for the most part by D , but by other influences such as velocity and turbulence.

As described by Heitz (24), when early interpretations of mass transfer were made, Nernst (25) believed in the existence of a stationary diffusion boundary-layer of a certain thickness on the surface, and outside it the flowing liquid. There was a sharp distinction between diffusive and convective transport. But, because this model could never be verified, in the last twenty years a general model has evolved which considers the existence of a hydrodynamic boundary layer (a velocity layer) which includes a diffusion zone, and also considers that flow in some way determines the diffusion boundary layer (in which the total change in concentration occurs).

Many experiments have been performed to determine the effective diffusion boundary layer and mass transfer by using devices such as rotating disks or cylinders (e.g., (18)), or tubes and channels (26, 27). Very few experiments have directly dealt with the case of the flat plate. The only extensive mathematical determination of mass transfer on a flat plate was performed by Wranglen and Nilson (20).

A useful non-dimensional parameter for the mass transfer is the Nusselt number, which is more often used in heat transfer problems than in mass transfer relations. The Nusselt number may be defined as follows:

$$(11) \quad Nu = j x/D(c_b - c_e)$$

where

- j = diffusion rate density ($\text{mol}/\text{cm}^2 \text{ sec}$)
- x = characteristic length (m)
- c = concentration (mol/m^3)
- b = bulk electrolyte
- e = electrolyte in contact with the electrode
- D = diffusion coefficient (m^2/sec).

By using the appropriate concentration profile Wranglen determined the equation for the Nusselt number in turbulent flow:

$$(12) \quad Nu = 0.17 Sc^{1/3} Re_x^{3/6}$$

which is of the general form $Nu = C Re^m Sc^n$, where the constants C , m and n depend on the flow configuration.

The Nusselt number is a measure of the relation of the mass transfer rate and the diffusional capability of a system, represented in equation (11) by j and $D \cdot \Delta c/x$ respectively. It is also a number which takes into consideration the hydrodynamic parameters (by including dependences on the flow structure through Reynolds number and on properties of the fluid through the Schmidt number (which includes the viscosity and the diffusivity)). An increase in D does not result in a higher Nusselt number, because the Nusselt number is not a direct measure of mass transfer; rather it is a measure of the relative magnitude of mass transfer relative to simple molecular diffusive mass transfer. Thus an increase in D will in fact correspond to a decrease in Nu , all other factors being the same. The relative importance of the various basic mechanisms of mass transfer (molecular and

convective diffusion) can be changed in equation (12) by varying the exponents m and n, depending on the flow system and the fluid involved. The corresponding relation in heat transfer is found by putting the Prandtl number instead of the Schmidt number into the equation, which yields the relation given by Holman (23).

Instead of the Nusselt number, mass transfer considerations often use the similar Sherwood number. The fundamental definition of the Sherwood number is (28):

$$(13) \quad Sh = h_d x/D$$

where h_d is the mass transfer coefficient (m/sec) comparable with h , the heat transfer coefficient. Because of the interchangeability of the Sherwood and Nusselt numbers, the Sherwood number can also be expressed in terms of two other non-dimensional parameters, the Reynolds and Prandtl (or Schmidt) numbers:

$$Sh = f(Re,Pr) \quad \text{or} \quad = f(Re,Sc).$$

Holman (23) gives a formula for h_d over a flat plate:

$$(14) \quad h_d = 0.0296 Re_x^{-1/6} U_0 Sc^{-2/3}.$$

Here the Sherwood number becomes:

$$(15) \quad Sh = 0.0296 Re_x^{-1/6} U_0 Sc^{-2/3} x/D.$$

By mathematical operations and simplifications one can get:

$$(16) \quad Sh = 0.0296 Re_x^{4/6} Sc^{1/3}$$

which is significantly different from the expression for Nusselt number given by Wranglen and Nilsson (20).

Another method to express diffusional flux is described by Levich (18) and by Holman (23). By using the local friction factor k_f , which varies as a weak function of distance x along a flat plate, the total diffusional flux can be written as:

$$(17) \quad I = b c_b U_0 / (1.4 \cdot a Pr^{3/4}) \int_0^L k_f^{1/2} dx$$

where

- b = width of the plate
- c_b = concentration of solution
- a = a constant to be determined by experiments, close to unity.

The factor k_f can be calculated by the relation:

$$(18) \quad 1/k_f^{1/2} = 4.1 \log_{10} (k_f Re) + 1.7$$

or by the Blasius relation:

$$(19) \quad k_f = 0.0396/Re^{1/4}$$

Substituting the total (integrated) drag coefficient K_f into the equation for I:

$$(20) \quad I = K_f^{1/2} c_b U_0 \text{ Area}/(1.4 \cdot a Pr^{3/4})$$

In a non-dimensional form this equation becomes:

$$(21) \quad Nu = K_f^{1/2} Re Pr^{1/4} / (1.41 a)$$

This is a relation for mass transfer written in terms of the friction factor, which determines the shear stress over a plate, and of two other parameters, the Reynolds and Prandtl numbers.

An important parameter in electrochemical situations is the limiting current density i_l . Newman (29) describes the limiting current density as the highest possible rate of mass transfer to the reacting surface. It is the amount of current which is able to be supplied to the surface, and like the Nusselt number, can often be used as a measure of the corrosion rate. The limiting current density can be described by the expression:

$$(22) \quad i_l = D n F c_b/d_d$$

where

- n = number of electrons transferred
- F = Faraday's constant .

Davis used the relation $Sc^{1/3} \cdot d_h/d_d$ to rewrite the equation:

$$(23) \quad i_l = D^{0.67} (n F c_b)^{0.12} U_0^{0.2} (0.38 L^{0.08}).$$

Since the present authors regard this relation of Schmidt number to be invalid for turbulent flow, the equation determined by Wranglen is taken into consideration:

$$(24) \quad i_1 = 0.143 Z F D c_b / ((1-n)x) Sc^{-1/3} Re_x^{0.6}$$

where

$$Z = \text{valence.}$$

As can be seen from this formula i_1 decreases with x . The physical explanation for this is that the solution in the diffusion boundary layer at a given point x has already been depleted by the reaction further upstream. On the other hand, i_1 will increase as the velocity increases, because the Reynolds number increases also.

The limiting diffusion current for oxygen is often the controlling cathodic process for corrosion in aerated aqueous electrolytes at lower and medium velocities. With increasing Reynolds number (typically greater than 10^6) the controlling process may shift to hydrogen evolution, as pointed out by Davis and co-workers (30 - 31), and above this Reynolds number increasing velocity would not be expected to have any further electrochemical effect (at least on the basis of oxygen provision), but very high velocity may result in a more pronounced mechanical component of the erosion-corrosion process. Newman (29) provides an excellent summary of limiting current densities and Nusselt numbers for different flow situations, such as those occurring with rotating disks, rotating cylinders, and flow channels.

The Sherwood number is a measure of the mass flux to a corroding surface, according to the relation:

$$(25) \quad Sh = \frac{x}{D \Delta c} j$$

Since the mass flux is an important factor relative to the corrosion process, it is of interest to calculate its theoretical value from its relation to the limiting current density:

$$(26) \quad j = \frac{i_1}{z \cdot F} .$$

Thus:

$$(27) \quad i_1 = Sh \frac{(D \Delta c)}{x} \cdot z \cdot F .$$

By using this equation it is possible to compare the maximum possible current density determined by the theory with actual experimental results, such as obtained in the present study. Assuming: $\Delta c_{O_2} = 10 \text{ ppm} = 3.1 \times 10^{-7}$

g mole/cm³, $D_{O_2} = 1.08 \times 10^{-5} \text{ cm}^2/\text{sec}$, $z = 1.1$, $F = 96500 \text{ coulombs}$, and

using the equation from Wranglen (20) for the Sherwood number,

$Sh = .17 Sc^{1/3} Re_x^{3/5}$, one obtains that the relation between Sh and i_j is $i_j = 7 \times 10^{-8} Sh$. The values of Sh for the experimental velocities 2, 4 and 6 m/sec are 1600, 2430, and 3100 respectively, and the corresponding values of i_j are determined to be:

$$i_j (2 \text{ m/sec}) = 114 \mu\text{A}$$

$$i_j (4 \text{ m/sec}) = 173 \mu\text{A}$$

$$i_j (6 \text{ m/sec}) = 220 \mu\text{A}.$$

These results are high relative to the measured current density of $12 \mu\text{A}/\text{cm}^2$, but one has to take into consideration that i_j is the maximum possible current density, and does not describe the actual polarization behavior of the material. In comparing the influence of velocity on these values, it is noted that the theoretical increase of i_j with velocity is relatively greater than the actual increase with velocity. For velocity ratios of 1:2:3 the actual current results have the ratios 1:1.17:1.33, whereas the theoretical i_j has the ratios 1:1.5:1.9, equivalent to the ratios of the Sherwood numbers. By using other theoretical relations for Sh than that of Wranglen, the ratios of theoretical i_j can be brought closer to the ratios of the velocities, but will be farther from the actual current results.

3. Possible Parameters for Corrosion Rate Correlations

It is clear that free stream velocity is not a sufficiently descriptive flow parameter to serve in a reasonable correlation between corrosion rate and the hydrodynamic variables which govern the erosion-corrosion process. Reynolds number can describe flow in various geometries, and includes one property of the fluid (the viscosity), but still does not sufficiently characterize both the fluid and the flow; for example, it does not include the turbulence intensity. If the Reynolds number is normalized by a critical Reynolds number (for turbulent transition in the specific geometry), additional

features of the flow are implicitly included in this new parameter. The critical Reynolds number is a measure of the point of flow in a specific geometry where the transition from laminar to turbulent flow occurs. Therefore, the ratio of these two Reynolds numbers represents the degree to which the flow situation exceeds the transition point. By including the critical Reynolds number in the correlation, variables like velocity, free stream turbulence, surface roughness, pressure gradient and tube diameter are effectively normalized, so that corrosion rate results plotted versus Re/Re_c should give more comparable data. Turbulence intensity is indirectly included in such a parameter, since such features as surface roughness and free stream turbulence are strong influencing factors for it. There is a practical problem, however, in the exact determination of the critical Reynolds number. There are many suggestions in the literature about methods to measure the laminar-to-turbulent transition, but it is obviously difficult to achieve an exact number in the gradual transition range, and the experimental methods are sophisticated and demand elaborate equipment and procedures.

The Sherwood number includes both flow structure and fluid property elements, so that some of the most important factors for corrosion of a given material in a flowing system are combined; the exact polarization behavior is not accommodated. If the turbulence intensity could also be introduced into a Sherwood number-type parameter this would seem to be a very effective parameter for corrosion/flow structure correlation. This introduction could be performed by using the sum of the molecular diffusion, as given by D, and the eddy diffusion, ϵ ; the latter can be related to the turbulence structure, and accommodated in the Schmidt number:

$$Sc = \frac{V}{D + \epsilon} .$$

The same was done for the mass flux equation (see equation (9)). However, there is no exact mathematical definition of ϵ from which its value can be predicted from known hydrodynamic parameters. The related parameter of theoretical mass flux, j , is basically the same parameter as the Sherwood number; j is a function of D and d_d , which both combine the same parameters as the Sherwood number: Sc and Re.

Some of the primary physical variables which must influence seawater corrosion under flow conditions are the average velocity, the local turbulence intensity, and the oxygen flux to the surface (some of these factors are mechanistically redundant). These three variables all increase with RPM in the

present tests. Further, one may argue that two basic mechanisms compete with each other to determine the net corrosion rate of Cu-Ni: (1) oxygen flux to the surface results in a higher dissolution rate and (2) the build-up of a corrosion product layer increases the resistance of the surface to oxygen penetration to the base metal.

Macdonald and co-workers (8) showed experimentally that an increase in oxygen content can cause a net decrease in corrosion rate, because the oxide layer (mainly Cu_2O) can grow faster and thicker. But at certain oxygen level the polarization resistance drops, resulting in an increase of the corrosion rate. This result apparently reproduces (at zero velocity) the familiar phenomenon of a "breakaway velocity", and shows that the occurrence of such a breakaway in corrosion rate with increasing velocity corresponds to the attainment of a critical level of oxygen mass transfer to the surface. The critical oxygen determined by Macdonald et.al. was about 7 ppm which is lower than the oxygen content of the electrolyte in the present work (10ppm). But even if the oxygen level were below the critical value, accelerated corrosion could be produced under flow conditions. This is because the bulk concentration of oxygen in the solution can be enhanced by flow. Substantial enhancement may be expected in flow situations with high turbulence, which will provide the surface of the metal locally with such a high value of O_2 that the critical value is easily exceeded. Therefore, the breakaway velocity is a function of bulk oxygen concentration. In the present experiments, it is apparent that the environment provided more than the critical oxygen concentration to the surface even at the lowest velocity, 2 m/sec; the break-away value of Cu-Ni is commonly stated to be about 4 m/sec.

Another aspect of high intensity turbulent flows is the local stresses which may be imparted to the surface. Although the average shear stress at the specimen for the velocities studied does not exceed 0.02 psi, which is clearly too small to have a significant effect on the adhesive Cu_2O corrosion product layer, the turbulence structure may locally develop much higher stresses, which may be strong enough to remove corrosion products. The non-uniform thickness of the product seen on some specimens in this study supports the idea that local stresses have some mechanical influence on corrosion. This effect may be considered a manifestation of the elusive mechanical component of the erosion-corrosion process. In this case it is not a process of direct removal of the base metal but rather an influence on a protective corrosion product layer, whose morphology is mechanically affected by the flow structure.

Therefore turbulent flows involve a complex combination of mechanisms which can influence corrosion rates: one basic aspect of the flow structure is that of mass transfer; the other aspect, which operates simultaneously, is one of local mechanical stresses imparted by the fluid to the surface. Even if it is assumed that the forces are not strong enough to wipe off the whole protective layer, one can easily conceive of a mechanism by which local turbulent forces remove small particles of corrosion product from the surface, with the result of a more porous layer. Non-uniform corrosion product layer thickness may be developed by mechanical influences, as seen on the surfaces of samples in this study (Figures 24, 25), resulting in locally different resistances to corrosion and causing a rougher surface. A locally rough surface results in turn in higher local turbulence, causing an even higher local stress. This process is obviously self-promoting, i.e., once initiated, the mechanical component will become more and more dominant as time goes on, and could conceivably remove all of a corrosion product layer.

Since the required shear stress for removal of surface layers is not known, and since the actual amplified local shear stresses are not known, the reasoning expressed above can only be hypothetical. A sophisticated experimental scheme may eventually be devised to measure these unknowns and prove these assumptions. However, there is clear physical evidence for mechanical effects of turbulent flow structure.

It is beyond the scope of the present report to analyse all possible parameters which may relate the corrosion rate or mass transfer rate to hydrodynamic parameters. There exist in the literature numerous alternative approaches to this problem that have not been covered in detail here. Tvarusko (32) tried to correlate ratios of the Schmidt and Sherwood numbers with different powers, and turbulence intensity, to corrosion rate. Van Shaw (33) applied the Stanton number, which can be expressed as $Nu/(Re Pr)$, or as mass transfer coefficient/velocity, to find a correlation in the entrance region of pipe flow. Cornet (26) researched the effect of Reynolds number on corrosion of copper in pipes, Ross (22) described general effects of electrolyte velocity, and Ellison (34) used a rotating disc to determine the equation for the Sherwood number.

Correlations between corrosion rate and parameters describing the whole system have not been completely successful, because it is difficult to determine the variables exactly by either theory or experiment. As

already mentioned, measurement of hydrodynamic variables demands sophisticated equipment, the application of which lies beyond the usual scope of corrosion science. A corrosion scientist who wants to include both the hydrodynamic and material aspects in theory and practice in a flowing system has to have extensive knowledge and experience in both fields. Advancement in both these aspects was one of the goals of this study.

SUMMARY AND CONCLUSIONS

One of the main interests we have had in this study has been in the area of hydrodynamic characterization of the flow field. Perhaps because of this bias, we find the phrase "velocity effects on corrosion," which is used commonly, to be superficially descriptive of the process of erosion-corrosion. This is because of the lack of correlation of corrosion rates with average velocity. A more accurate phase might be "flow effects on corrosion," or even "effects of flow structure on corrosion." If you are mounting samples inside a pipe and pumping electrolyte past them and measuring weight loss as a function of flow rate, with no flow characterization other than a measure of the volume of water discharged per unit time, then you obviously cannot relate results to other than the apparent average velocity; this is indeed an (average) velocity effects study.

But at the same time, this is exactly the situation in which it is least appropriate to cite the average velocity to describe the flow situation, because of the complex, virtually uncharacterizable situation created by the experimental geometry. Deploying a blunt sample in a pipe creates a severe disturbance to flow, probably including cavitation phenomena, intense turbulence, and other features that are impossible to predict or model. On the other hand, if a hydrodynamically "clean" apparatus is used, citing only the average velocity is a lesser sin, since you can at least estimate other flow parameters using basic fluid dynamics expressions (e.g., Reynold's number, etc.).

Furthermore, if the trouble is taken to experimentally characterize the flow structure near the corrosion samples, such as by measuring flow rate, velocity profiles, turbulence intensity, or by flow visualization, then you are approaching the fundamental ideal of complete flow characterization. Clearly, corrosion engineers cannot be troubled with excessive

procedures in this regard, but it is also clear that "velocity effects" data will be much more readily (and usefully) transferred from one flow situation to another (including the crucial transfer from the experimental station to actual service) if there is better knowledge of the flow structure.

Since it seems clear that the mechanisms of erosion-corrosion are intimately connected to some of the fundamental parameters of fluid dynamics, it might at least be good form for corrosion scientists to use experimental designs which would satisfy the minimum requirements for a sound fluid dynamics study, i. e., proper lead-in sections, no abrupt changes in cross-section, streamlined sample deployment, no abrupt protrusions in the flow field, etc. Furthermore, when reporting results of velocity effects experiments, it is not sufficient to simply report the nominal relative velocity as the independent variable as historically has been done. It is necessary to cite at least, the geometry of the system, e. g., the tube size, etc., and recognize that the data is otherwise only internally consistent to the experiment.

If corrosion rate is to be predicted through a hydrodynamic/electrochemical model, we still need to decide what parameters are to be included in the model. One approach, thus far not advanced, is to use turbulence intensity (or related structural parameters such as eddy size) directly, rather than incorporating the flow structure in only an indirect way, via dimensionless parameters such as Re , Sc , and Sh . Several quantities which can be fairly easily obtained experimentally are: (1) the maximum turbulence intensity, U'/\bar{U} , (2) the characteristic distance, y , from the wall at which the turbulence intensity peak occurs, (3) the microscale of turbulence, λ . These measures might be cast in the form of a nondimensional grouping, forming a parameter which we might assume would bear a direct relationship to corrosion rate, i.e., as U'/\bar{U} increases (more violent flow), and as λ decreases (smaller eddies), and y decreases (high turbulence closer to the wall), the corrosion rate should increase. There is certainly some redundancy in this grouping, however. Also, the properties of the fluid are not reflected. Viscosity might be included in some way, for example; higher viscosity would tend to give lower turbulence intensity for the same velocity and geometry. Since the tendency to turbulence would be damped by viscous forces; this would then correspond to lower corrosion rate. Also, a measure of the frequency of the fluctuations in U' might be included, f . Clearly, the search for this elusive model parameter will require further work.

Regarding the mechanical influence of turbulent flows in the erosion-corrosion process, several authors have mentioned that the wall shear stress due to a high velocity flow is negligible, usually calculated to be only a small fraction of a psi. The inference is that there cannot be any mechanical influence of flow if the stress is so low. Unfortunately, these authors are referring to the average wall shear stress, a macroscopic parameter which is totally irrelevant to the erosion-corrosion process. Average shear stress is a macroscopic parameter in that it totally neglects flow structure in turbulent flow fields. It cannot account for the local forces imparted to the wall by the eddy microstructure of turbulent flow fields. In intense flows, these forces can definitely be expected to play a mechanical role in the erosion-corrosion process (as well as playing an electrochemical role relative to the eddy diffusivity component of mass transfer).

In summary, the following points may be made on the basis of theoretical considerations in this work:

1. The relation $d_h/d_d = Sc^{1/3}$ is not valid for turbulent flow.
2. Taking the shape of the various curves for the development of boundary layers into account, the equation for d_d due to Wranglen and Nilson (20) seems more reasonable than others mentioned in the literature.
3. The opinion often found in the literature that a decrease in the diffusion boundary layer thickness, d_d , generally results in enhanced mass transfer rate is only valid when the change in d_d is not completely determined by a change in the diffusion coefficient D. The idea that lowering d_d represents an increase in mass transfer rate is valid when the decrease in d_d results from an increase in flow.
4. There are two basic mass transfer mechanisms: convective diffusion and molecular diffusion. The ratio of these is given by the Sherwood (or Nusselt) number. Since a flow electrolyte transports mass mostly via the former mechanism, the Sherwood number represents a useful measure of the enhancement of electrochemical reactions by the flow field.
5. The Sherwood (or Nusselt) number is a reasonable non-dimensional parameter for correlation with corrosion rate, because both the hydrodynamic (flow) properties, as given by the Reynolds number (U, x), and the fluid and diffusion properties as given by the Schmidt number (ν, D) are combined. An even better correlation could be gained if it were possible to determine the additional convective diffusivity term caused by turbulence, and add this value, represented by ϵ , to the molecular diffusion

coefficient D in the equation for the Schmidt number, as $S_c = v / (D + \epsilon)$. By this method the effect of the particular level of turbulence intensity could effectively be included in the Sherwood number and the same could be achieved in the equation for mass transfer, as $j = (D + \epsilon) \Delta c / d_d$.

6. A normalized Reynolds number parameter, Re/Re_{cr} , is another promising parameter for correlation with corrosion rate, which implicitly includes many flow features, but probably does not sufficiently represent fluid properties.

7. Higher turbulence intensity probably decreases the critical break-away velocity, because of the enhanced transport of oxygen provided by the more intense flow structure.

8. These are clearly both electrochemical and mechanical influences of high-intensity turbulent flows. Average surface shear stress is a meaningless parameter relative to the microscopic processes of erosion-corrosion, but local fluctuations in surface stresses due to high intensity flow structure may be many orders of magnitude higher.

LIST OF REFERENCES

1. Jeff Perkins, K. J. Graham, G. A. Storm, J. S. Locke, and J. R. Cummings, "Effects of Velocity on Corrosion of Galvanic Couples in Seawater," Paper No. 26, Corrosion/78, Nat'l Assoc. Corros. Eng., Houston, Texas, March 1978.
2. B. C. Syrett, "Erosion-Corrosion of Copper-Nickel Alloys in Seawater and Other Aqueous Environment - A Literature Survey," Corrosion 32 (1976) 242.
3. R. P. Schack, G. Leumer, K. J. Graham, and J. Perkins, "The Effects of Flow Structure on Corrosion: Flow Channel Studies on 90/10 Copper-Nickel," Naval Postgraduate School Technical Report NPS-69PS-78-003 Technical Report No. 7 to the Office of Naval Research, Contract No. N00014-78-WR-80105, NR-036-120, April 1978.
4. J. Perkins, W. H. Luebke, K. J. Graham, and J. M. Todd, "Anodic Corrosion of Zinc Alloys in Seawater," J. Electrochem. Soc. 124 (1977) 819.
5. Kester et al, "Preparation of Artificial Seawater," Limnology and Oceanography, 12, (1967) 176.
6. M. Stern and A. L. Geary, "Electrochemical Polarization Theoretical Analysis of the Shape of Polarization Curves," J. Electrochem. Soc., 104 (1957) 56.
7. E. Pye, Report C-10, Practical Considerations in Performing Linear Polarization Measurements, Alpha Research.
8. D. D. Macdonald, B. C. Syrett, and S. S. Wing, "Methods for Measuring Corrosion Rates of Copper Nickel Alloys in Flowing Seawater, Paper No. 25, Corrosion/78, Nat'l Assoc. Corros. Eng., March 1978, Houston, Texas.
9. G. Lauer, and F. Mansfeld, "Technical Note: Measurement of Galvanic Corrosion at Zero External Impedance," Corrosion, 26 (1970) 185.
10. J. Devay, et al, "Anwendung des Potentiostat zur Bestimmung des maximalen Korrosionsstroms von galvanischen Elementen," Acta Chemica Acad., Sci. Hungaricae, Tomus 62 (1969) 157-162.
11. J. O. Hinze, Turbulence, 2nd Edition, McGraw-Hill, 1975.
12. TSI (Thermo System Incorporated), Manual TSI, Section III, Theory and Application, 1973.
13. J. M. Popplewell, "Marine Corrosion of Copper Alloys, An Overview," Paper No. 21, Corrosion/78, Nat'l Assoc. Corros. Eng., March 1978, Houston, Texas.
14. CRC Handbook for Applied Engineering Science, 2nd Edition, CRC Press.
15. G. Bianchi, and P. Longhi, Corros. Sci., 13 (1973) 153.

16. F. Feigl, Spot Tests in Inorganic Analysis, Elsvier Publishing Company, 1958, p. 305.
17. R. G. Blundy, and M. J. Pryor, "The Potential Dependence of Reaction Product Composition of Copper-Nickel Alloys," Corros. Sci. 12 (1972) 65.
18. V. G. Levich, Physicochemical Hydrodynamics, Prentice Hall, 1962.
19. H. Schlichting, Boundary Layer Theory, McGraw Hill, 1968.
20. G. Wranglen and O. Nilson, "Mass Transfer under Forced Laminar and Turbulent Convection at Horizontal Plane Plate Electrodes, Electrochim. Acta, 7, (1962) 121-137.
21. E. Ecker, Einführung in den Stoff-und Wärmeaustausch, Springer Verlag, 1959, p. 73.
22. T. K. Ross, and B. P. L. Hitchen, "Some Effects of Electrolyte Motion During Corrosion," Corros. Sci. 1 (1961) 65.
23. J. P. Holman, Heat Transfer, 4th Edition, McGraw Hill, 1976, p. 435.
24. E. Heitz, "Untersuchung von Transportvorgängen bei der Korrosion," Werkstoffe und Korrosion, 15 (1964) 63.
25. W. Nernst, Z. Phys. Chem. 47 (1904) 56.
26. I. Cornet, E. A. Barrington, and G. U. Berhrsing, J. Electrochem. Soc., 108 (1961) 947.
27. D. Landolt, "High Rate Anodic Dissolution of Copper," J. Electrochem. Society, (1969).
28. T. K. Ross, and D. H. Jones, "Corrosion Inhibition in Moving Media," J. Appl. Chem. 12 (1962) 314.
29. J. Newman, "Mass Transport and Potential Distribution in the Geometries of Localized Corrosion," Localized Corrosion, Nat'l Assoc. Corros. Eng., 1974, pp. 45-61.
30. J. A. Davis, A. A. Watts and G. A. Gehring, Jr., "Pitting Behavior of Aluminum Alloys in High Velocity Seawater," presented at 150th Annual Conference of Electrochemical Society, Oct. 1976, Las Vegas, Nevada.
31. J. A. Davis, and G. A. Gehring, Paper No. 78 presented at Corrosion/74, Nat'l Assoc. Corros. Eng., March 1974, Chicago, Illinois.
32. A. Tvarusk, "Mass Transfer on Horizontal Wires in the Presence of Free and Combined Forced and Free Convection," J. Electrochem. Soc., (1976) 490.
33. P. V. Shaw and T. J. Hanratty, "Rates of Turbulent Transfer in a Pipe Wall in the Mass Transfer Entry Region," A.I.Ch.E. J., 10 (1964) 475.
34. B. T. Ellison and I. Cornet, "Mass Transfer to a Rotating Disk," J. Electrochem. Soc. 1185 (1971) 68.

LIST OF TABLES

Table I: Specification of 90/10 Cu-Ni Alloy (CDA 706)

Table II: List of Experiments

Table III: Hot-film Anemometry Results

Table IV: Corrosion Rate Results

Table V: Possible Corrosion Product Compounds

Table I: Specification of 90/10 Cu-Ni Alloy (CDA 706)

Constituents:	wt.%
Copper	87.4
Nickel	10.4
Iron	1.5
Manganese	0.49
Zinc	0.13
Silicon	0.02
Tin	0.02
Phosphorus	0.013
Lead	0.01
Sulphur	0.001

Table II: List of Experiments

Run	Time (hr)	Velocity (m/sec)	Measurements	Remarks
1	24	2	WL, LPM, ZRA	galvanic couple
2	24	2	WL, LPM, ZRA	galvanic couple
3	24	4	WL, LPM, ZRA	galvanic couple
4	4	4	LPM, ZRA	small galvanic couple
5	20	6	WL, LPM, ZRA	galvanic couple
6	24	2	WL, LPM	single metal, 2 specimens
7	48	4	WL, LPM*	single metal, 2 specimens
8	45	6	WL, LPM*	single metal, 2 specimens, LPM only for first 3 hours
9	0.5	2	LPM, ZRA	galvanic couple, short test for transient behavior
10	0.5	4	LPM, ZRA	galvanic couple, short test for transient behavior
11	0.5	6	LPM, ZRA	galvanic couple, short test for transient behavior
12	0.5	6	LPM, ZRA	galvanic couple, short test for transient behavior
13	22	Static	WL, LPM	single metal, 1 specimen
14	45	2	WL	single metal, 1 specimen
15	24	4	WL, LPM	single metal, 1 specimen
16	24	6	WL, LPM	single metal, 1 specimen
17	24	2	WL, LPM	single metal, 1 specimen
18	24	6	WL, LPM	single metal, 1 specimen

Runs 19 to 24 were shorter runs using only LPM to determine initial transient behavior.

Several more runs were performed to obtain potentiodynamic polarization curves at 2 m/sec, 4 m/sec and 6 m/sec.

WL: weight loss
 LPM: linear polarization method
 ZRA: zero-resistance ammeter

*LPM data in runs 7 and 8 aborted because of electrical connection problems.

Table III: Hot Film Anemometry Results

<u>Distance from Surface</u>	<u>Velocity</u>	<u>U'/\bar{U}</u>
15 mm	2 m/sec	0.036
	3 m/sec	0.045
	4 m/sec	0.054
	4.7 m/sec	0.063
1.5 mm	2 m/sec	0.24
	3 m/sec	0.197
	4 m/sec	0.21
	3 m/sec	0.203
	2 m/sec	0.238
1 mm	2 m/sec	0.326
	3 m/sec	0.247
	4 m/sec	0.26
	3 m/sec	0.253
	2 m/sec	0.302

Table IV: Corrosion Rate Results

Speed m/sec	SM or GC	Time (hrs)	Run #	WL		i _{corr}	LPM	
				Rmpy	Rumpy		Rmpy	Rumpy
2 m/sec	SM	24	6	5.6	143	9.2	7.6	193
	SM	45	14	7.4	189	-	-	-
	SM	24	17	8.7	220	10.0	8.3	210
	GC	24	1	-	-	7.7	6.4	163
	GC	24	2	-	-	6.3	5.2	132
4 m/sec	SM	48	7	8.5	216	-	-	-
	SM	24	15	7.4	188	12.0	9.9	250
	GC	24	3	-	-	7.5	6.2	157
	SM	24	16	10.8	275	13.0	10.7	272
6 m/sec	SM	24	18	8.9	221	14.0	11.5	292
	SM	45	8	8.7	221	-	-	-
	GC	20	5	-	-	7.5	6.2	159

SM: single metal exposure

GC: galvanic couple exposure; disconnected for LPM measurements

Table V: Possible Corrosion Product Compounds

Copper-based products:

Oxides:

cuprous oxide, natural cuprite	Cu_2O	(red)
cupric oxide, natural tenorite	CuO	(black)
peroxide	$\text{CuO}_2 \cdot \text{H}_2\text{O}$	(brown or brownish black)

Chlorides:

hydroxychloride	$\text{CuCl}_2 \cdot 3\text{Cu}(\text{OH})_3$	(green)
cuprous chloride	CuCl	(brown)

Sulfides:

cupric sulfide	CuS	(black)
----------------	--------------	---------

Nickel-based products:

nickel oxide	NiO	(green black)
--------------	--------------	---------------

LIST OF FIGURES

Figure 1: Circling-foil exposure tank and associated equipment, and electrochemical instrumentation set up for LPM measurements.

Figure 2: Cross-section diagram of circling-foil apparatus (see legend).

Figure 3: Specimen-carrying foil and streamlined strut for deployment from rotating arm in apparatus. Note specimen recesses (one occupied, one empty) and electrical lead to them.

Figure 4: Full-size plan drawings of specimen-carrying foil (all dimension in cm).

Figure 5: Close-up views of exposure tank, showing anti-stirring baffles.

Figure 6: Schematic top view drawing showing the arrangement of the foil with respect to the vertical strut, the horizontal rotating arm, and the path of specimen travel.

Figure 7: Drive system and electrical connections.

Figure 8: Basis of LPM measurements. Potential is varied by about ± 10 mV to the corrosion potential and the resultant current measured. The slope of the curve, $\Delta I/\Delta E$, in this region gives the polarization resistance, R_p , which may be converted to the corrosion current through the Stern-Geary relationship.

Figure 9: Equipment used for LPM measurements: potentiostat, programmer, x-y recorder.

Figure 10: Zero-resistance ammeter (ZRA) circuit diagram.

Figure 11: Equipment used for ZRA measurements: circuit box, digital voltmeters and stripchart recorder.

Figure 12: Equipment for hot-film anemometric measurements, DC power controller for drive system, rpm counter.

Figure 13: Arrangement of hot-film probe over specimen position in foil.

Figure 14: Anemometric data plotted to determine V_o ; corresponding to the data in Table III.

Figure 15: Actual LPM results for 90/10 Cu-Ni at velocities of 1.8, 3.3, 5.0, and 6.3 m/sec.

Figure 16: LPM-determined corrosion rates versus time for 90/10 Cu-Ni at 2 m/sec.

Figure 17: LPM-determined corrosion current density versus time for 90/10 Cu-Ni at 4 m/sec.

Figure 18: LPM-determined corrosion current density versus time for 90/10 Cu-Ni at 6 m/sec.

Figure 19: Comparison of the LPM-determined corrosion current density and the WL-determined apparent average corrosion current density for 90/10 Cu-Ni at 2, 4, and 6 m/sec.

Figure 20: Potentiodynamic polarization curve for 90/10 Cu-Ni at 2 m/sec. Sample surface area = 2.85 cm².

Figure 21: Potentiodynamic polarization curve for 90/10 Cu-Ni at 4 m/sec. Sample surface area = 2.85 cm².

Figure 22: Potentiodynamic polarization curve for 90/10 Cu-Ni at 6 m/sec. Sample surface area = 2.85 cm².

Figure 23: ZRA-determined galvanic current density versus time for 90/10 Cu-Ni: Pt (area ratio 1:30) couples at 0, 2, 4, and 6 m/sec.

Figure 24: As-exposed surface of 90/10 Cu-Ni sample after 24 hr. exposure in galvanic couple with Pt (area ratio 1:30) at 6 m/sec. (a) Light micrograph, 10X, (b) SEM micrograph, 500X, (c) SEM micrograph, 2000X.

Figure 25: As-exposed surface of 90/10 Cu-Ni sample after 24 hr. exposure in galvanic couple with Pt (area ratio 1:30) at 4 m/sec. Light micrographs (a) 100X, (b) 400X.

Figure 26: Polished and etched metallographic view of the microstructure of the 90/10 Cu-Ni sample material. 400X.

Figure 27: SEM view of cleaned surface of 90/10 Cu-Ni sample after 24 hour exposure in galvanic couple with Pt (area ratio 1:30) at 6 m/sec (a) 500X, (b) 2000X.

Figure 28: Light microscope views of cleaned surface of 90/10 Cu-Ni sample after 24 hour exposure in galvanic couple with Pt (area ratio at 4 m/sec. (a) 200X, (b) 400X.

Figure 29: Cleaned surfaces of samples of 90/10 Cu-10 after single metal exposures for 24 hours at (a) 6 m/sec, 100X, (b) 2 m/sec, 400X. Light microscope views.

Figure 30: SEM views of cleaned surfaces of 90/10 Cu-10 samples after single metal exposure for 48 hours at (a) 2 m/sec, (b) 6 m/sec. Both 2000X.

Figure 31: SEM views of cleaned surfaces of 90/10 Cu-Ni samples after single metal exposures for 48 hours at (a) 2 m/sec, (b) 6 m/sec. Both 500X.

Figure 32: SEM view of as-exposed surface of 90/10 Cu-Ni single metal. Sample after static exposure for 72 hours. 500X.

Figure 33: Schematic of boundary layers in turbulent flow, and the velocity profile across the boundary layers.

d_h = hydrodynamic boundary layer

d_{s1} = viscous sublayer

b.z. = buffer zone

$d_h - b.z. - d_{s1}$ = turbulent region of boundary layer

d_d = diffusion boundary layer

U_∞ = free stream relative velocity

Figure 34: Calculated boundary layer development along a flat plate according to the indicated formulae.

Figure 35: Calculated boundary layer development along a flat plate according to the indicated formulae. Scales expanded from those of Figure 34.

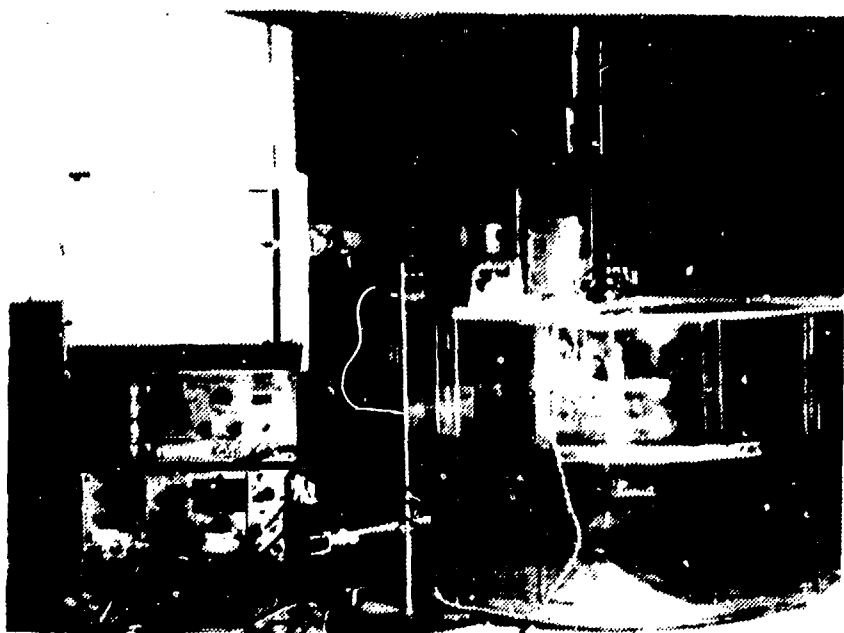


Figure 1: Circling-foil exposure tank and associated equipment, and electrochemical instrumentation set up for LPM measurements.

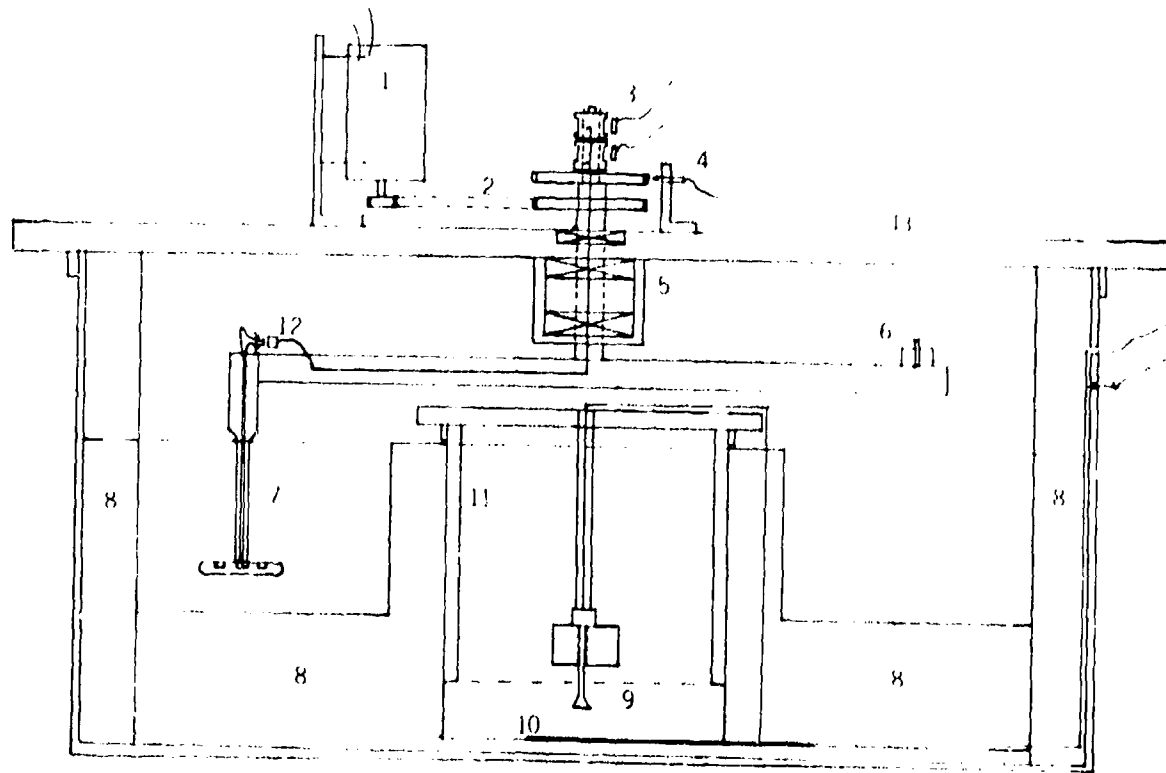


Figure 2: Cross-section diagram of circling-foil apparatus (see legend).

1. = 1/4 Hp controllable DC-motor
2. = driving belt arrangement including two pulleys in the ratio 1:4 and timing belt
3. = slip rings and brushes
4. = toothed wheel and magnetic sensor
5. = set of three bearings for main shaft
6. = counter weight for balance
7. = vertical strut and foil
8. = baffle system
9. = reference electrode (Ag-AgCl)
10. = counter electrode (Pt)
11. = hollow cylinder to hold baffles and RE
12. = electrical wiring system
13. = tank cover

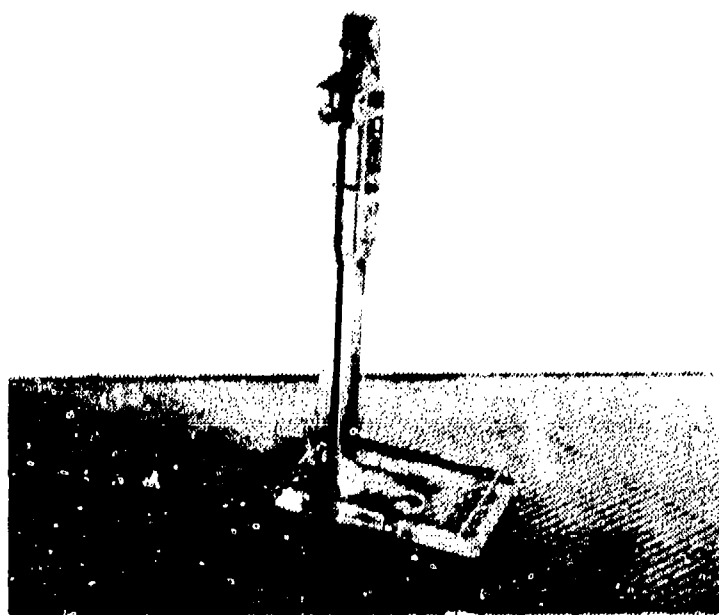


Figure 3: Specimen-carrying foil and streamlined strut for deployment from rotating arm in apparatus. Note specimen recesses (one occupied, one empty) and electrical lead to them.

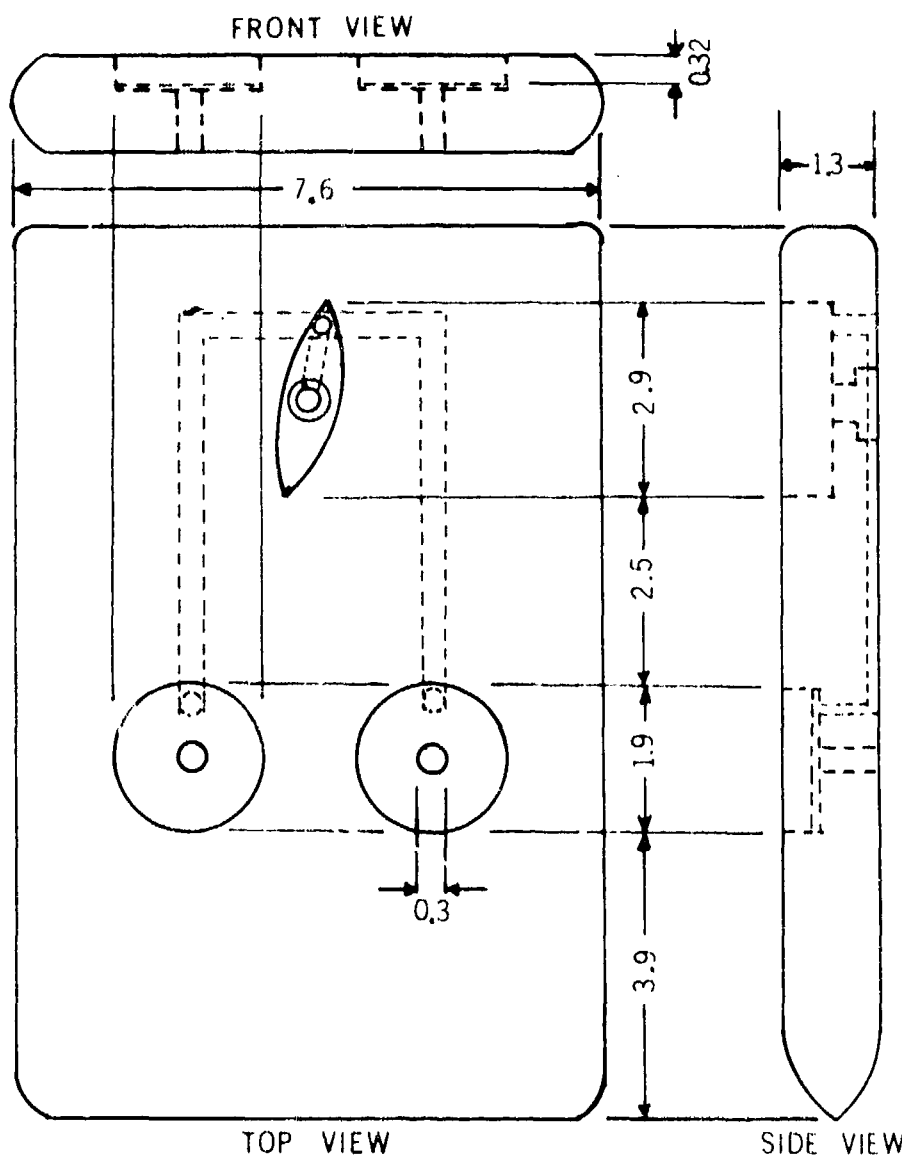


Figure 4: Full-size plan drawings of specimen-carrying foil (all dimension in cm).

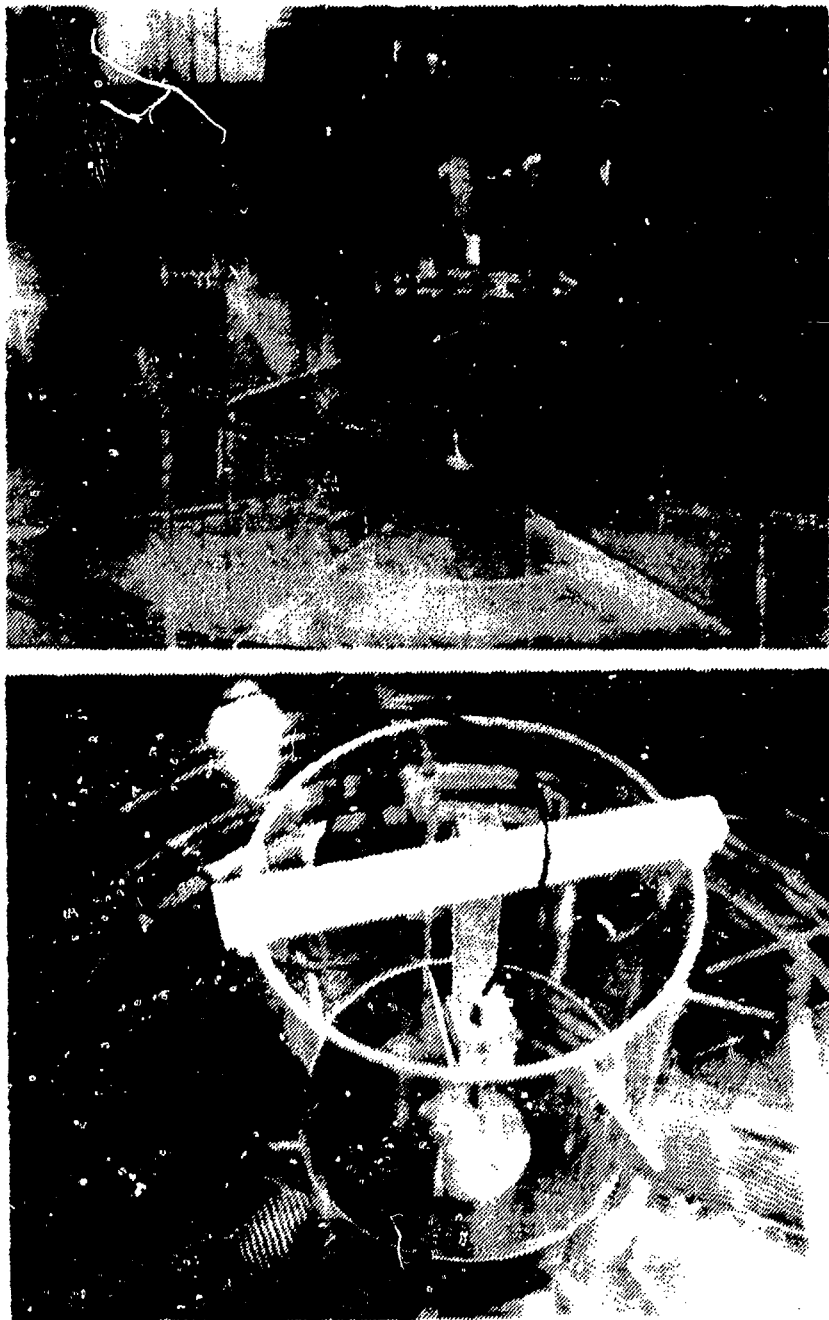


Figure 5: Close-up views of exposure tank, showing anti-stirring baffles.

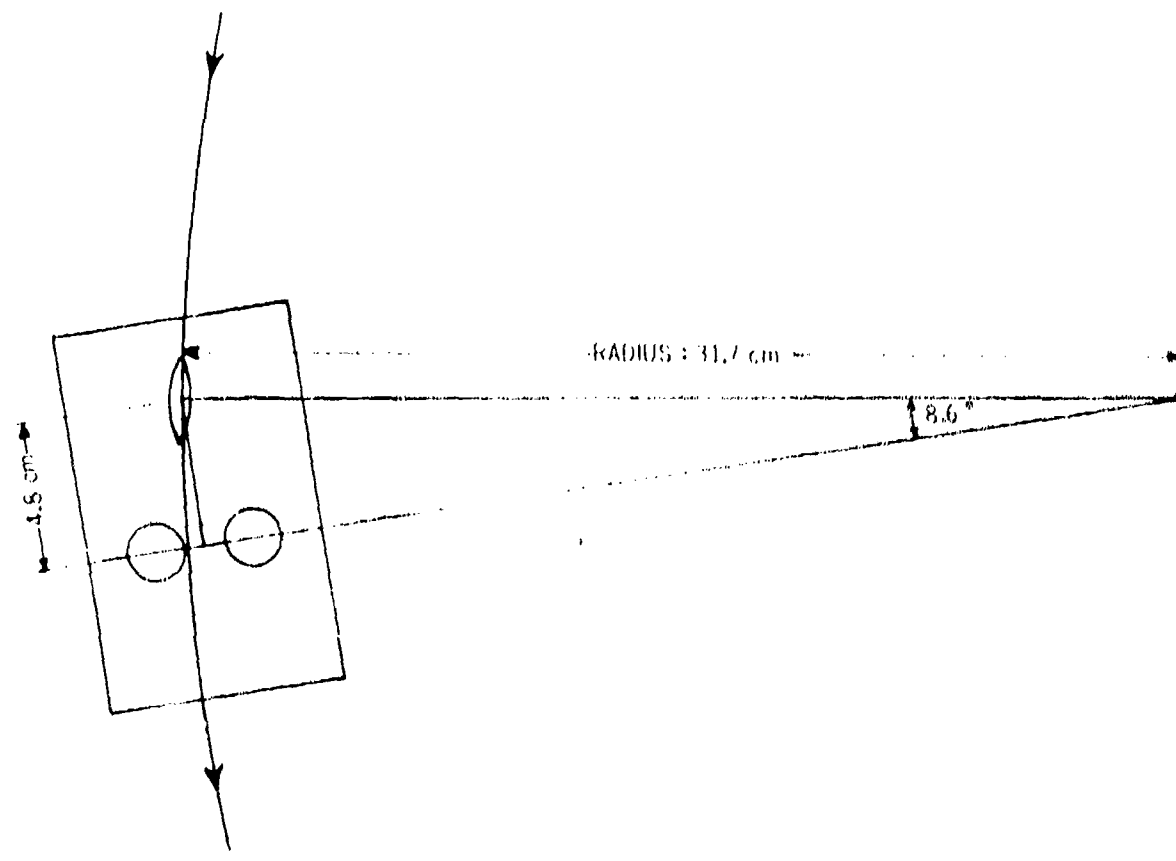


Figure 6: Schematic top view drawing showing the arrangement of the foil with respect to the vertical strut, the horizontal rotating arm, and the path of specimen travel.

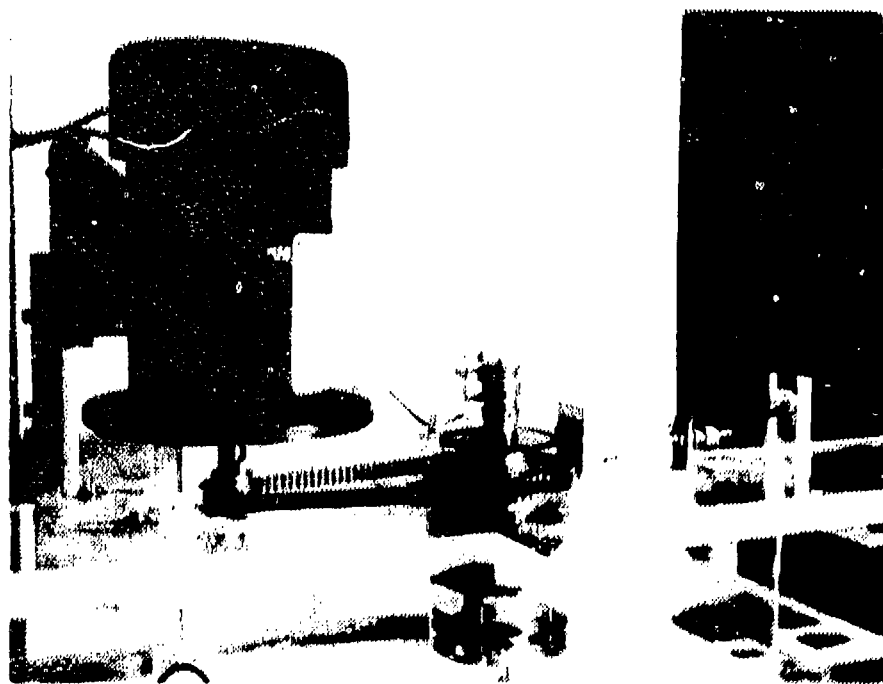


Figure 7: Drive system and electrical connections.

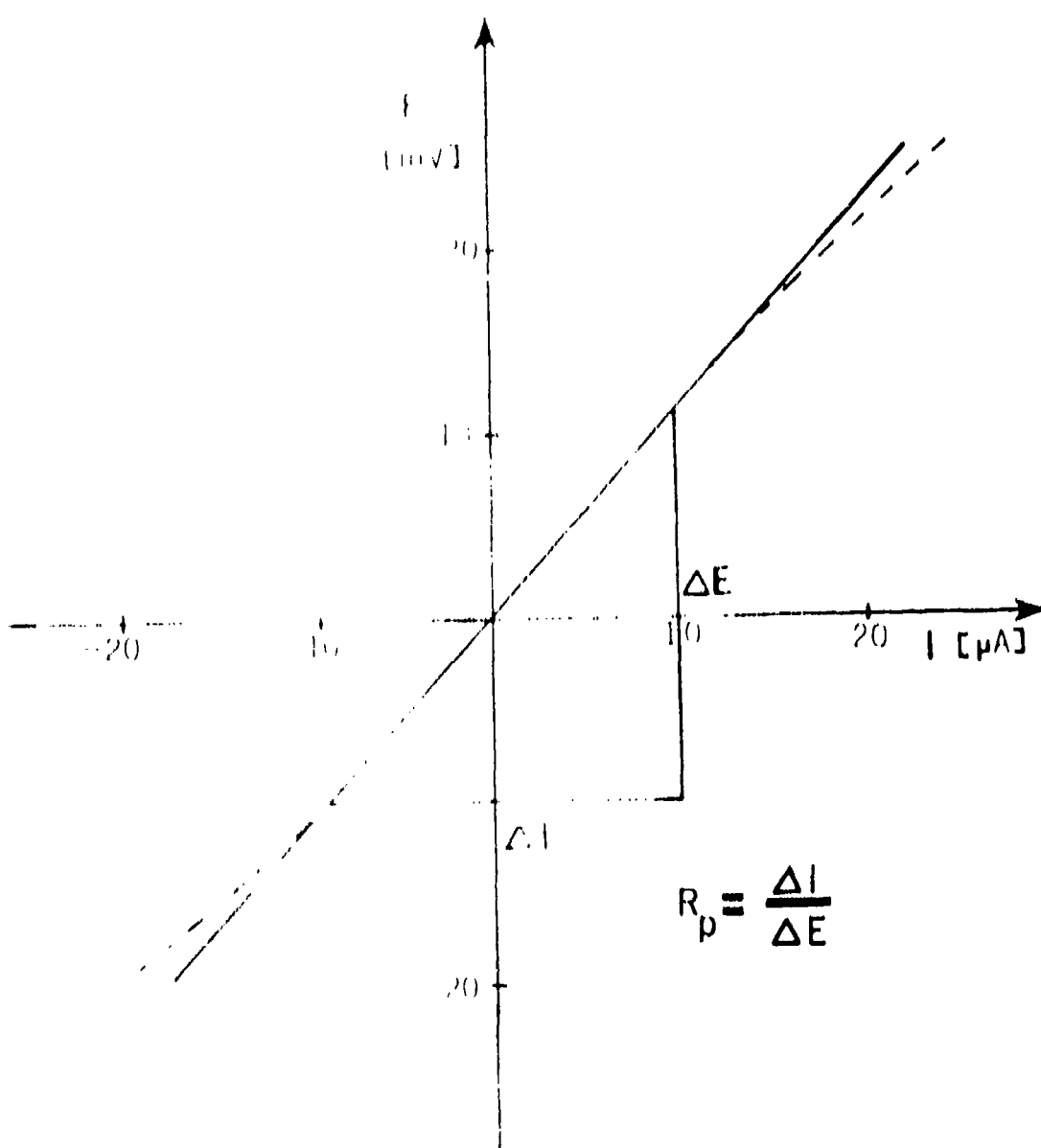


Figure 8: Basis of Tafel polarization. Potential is varied by about ± 10 mV to the corrosion potential and the resultant current measured. The slope of the curve, $\Delta I/\Delta E$, in this region gives the polarization resistance, R_p , which may be converted to the corrosion current through the Tafel-Nernst relationship.

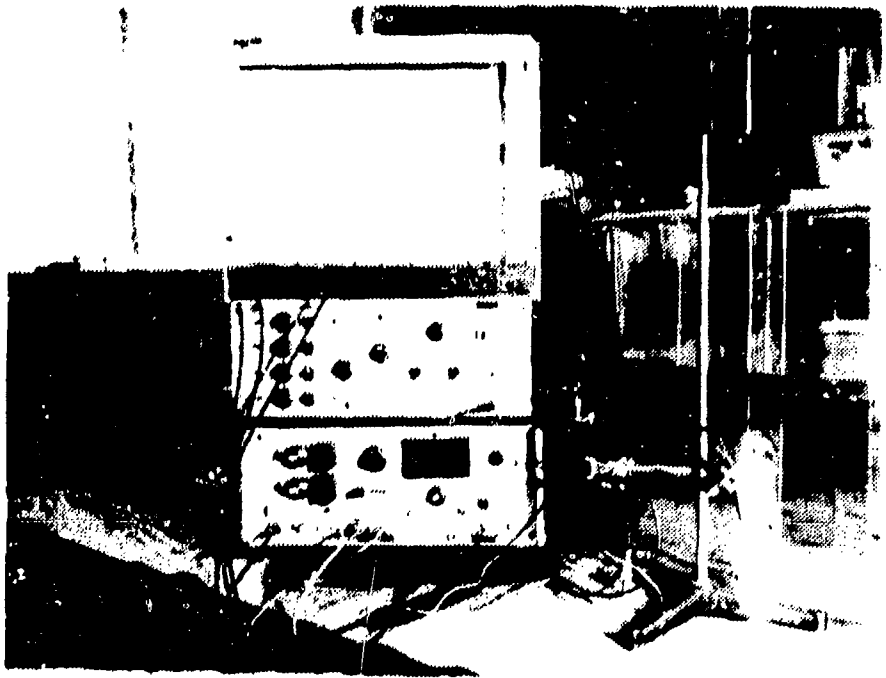


Figure 9: Equipment used for LPM measurements: potentiostat, programmer, x-y recorder.

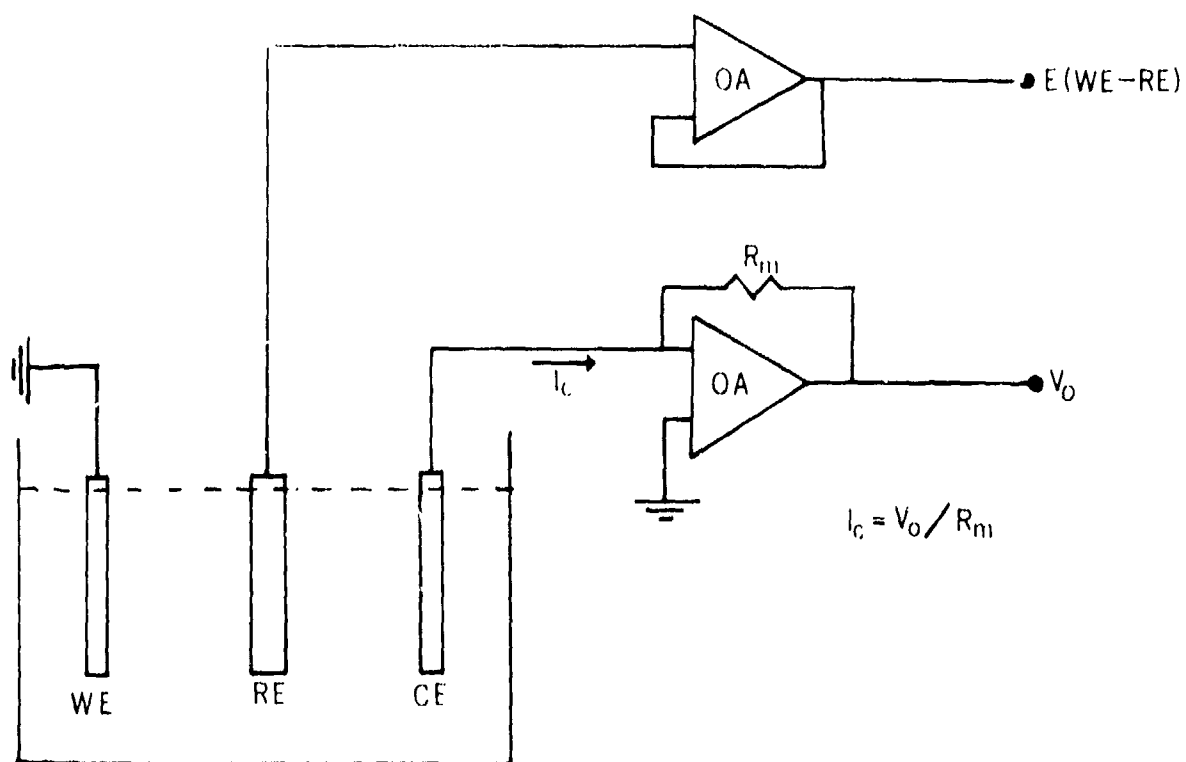


Figure 10: Zero-resistance ammeter (ZRA) circuit diagram.

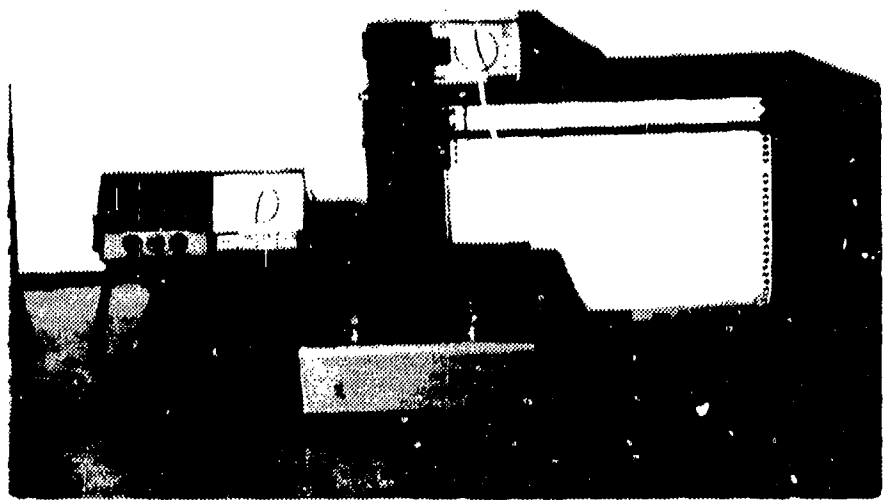


Figure 11: Equipment used for ZRA measurements: circuit box, digital voltmeters and stripchart recorder.

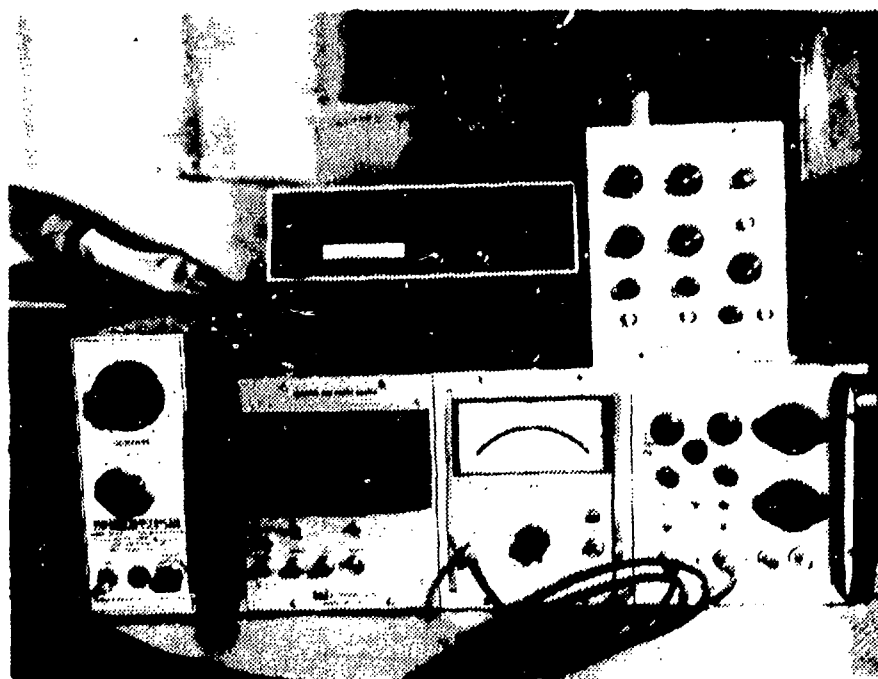


Figure 12: Equipment for hot-film anemometric measurements, DC power controller for drive system, rpm counter.

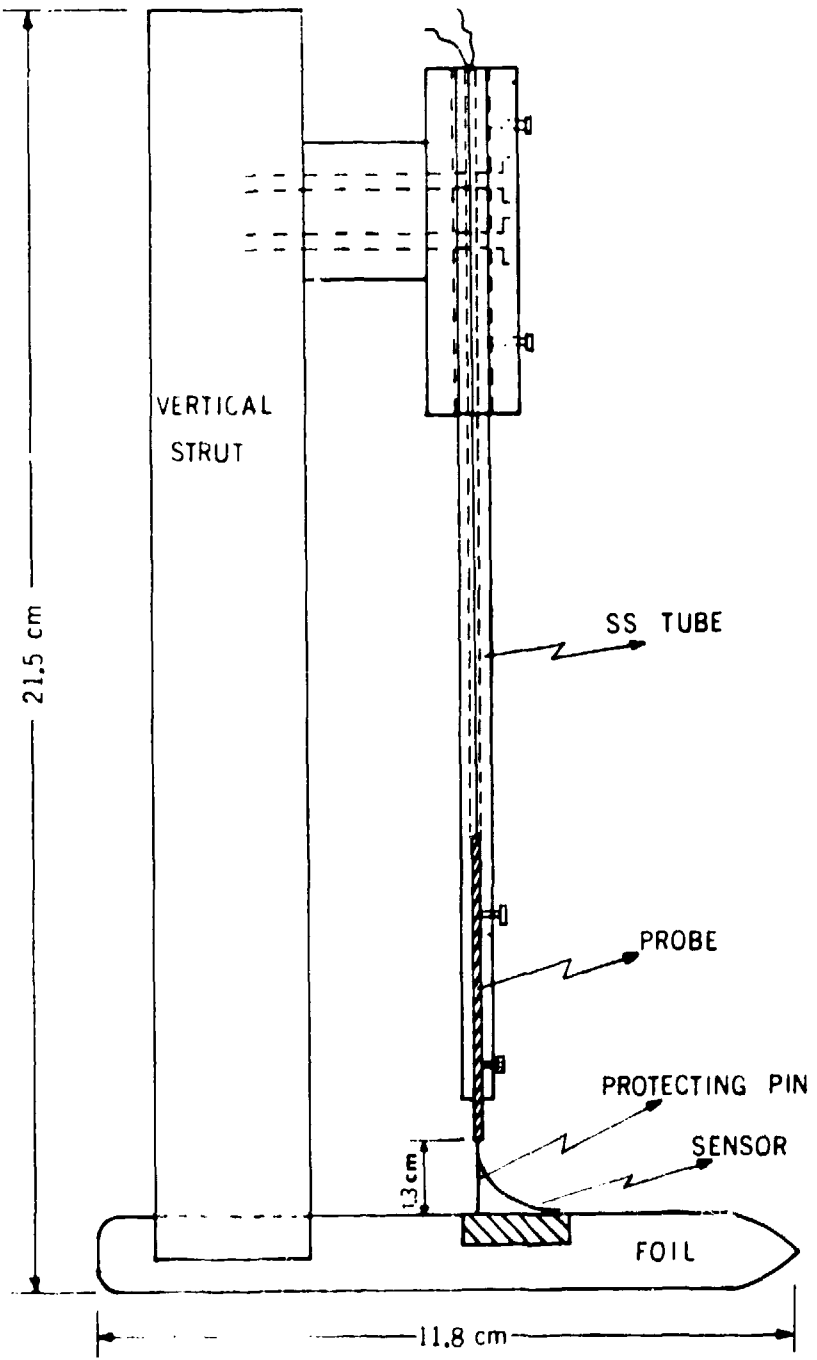


Figure 13: Arrangement of hot-film probe over specimen position in foil.

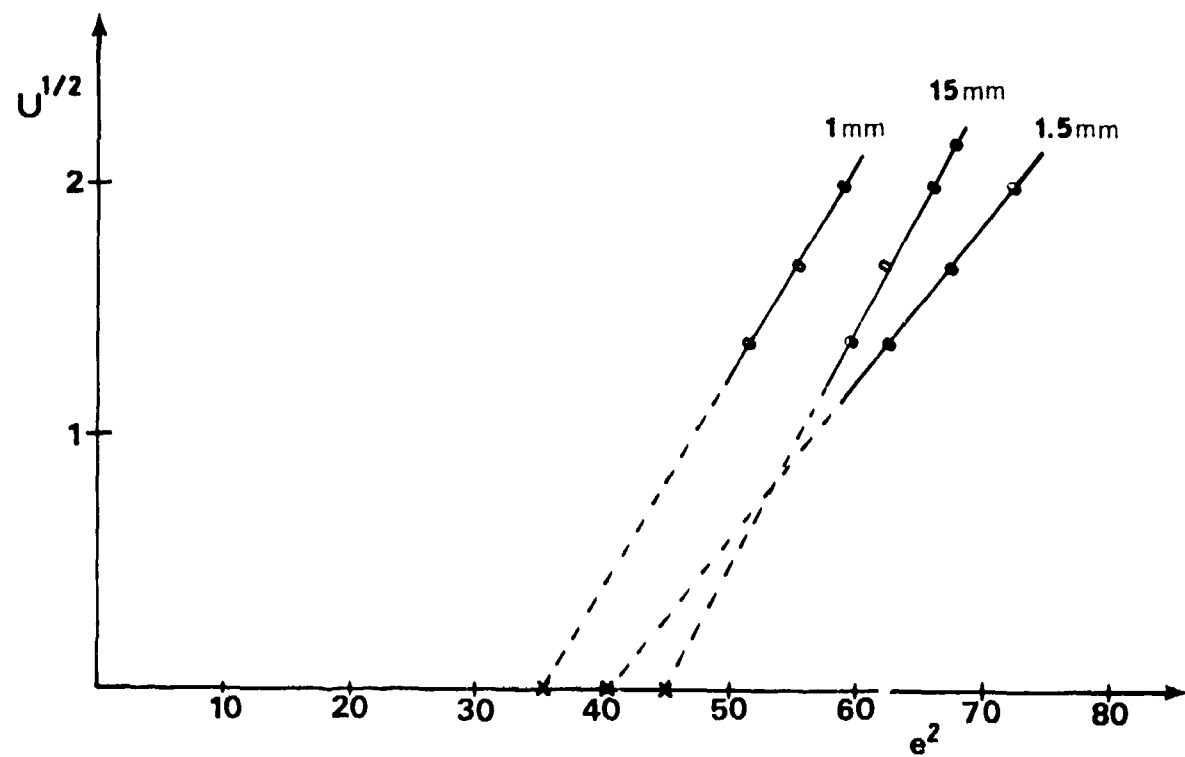


Figure 14: Anemometric data plotted to determine V_0 ; corresponding to the data in Table III.

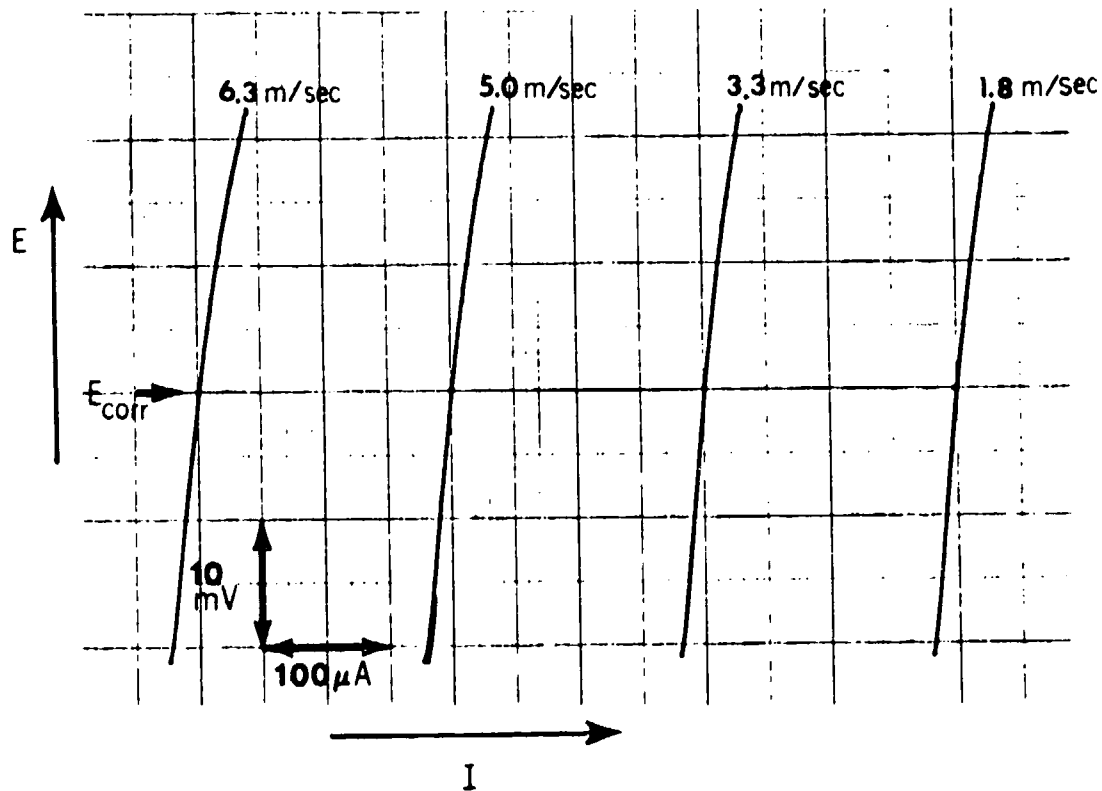


Figure 15: Actual LPM results for 90/10 Cu-Ni at velocities of 1.8, 3.3, 5.0, and 6.3 m/sec.

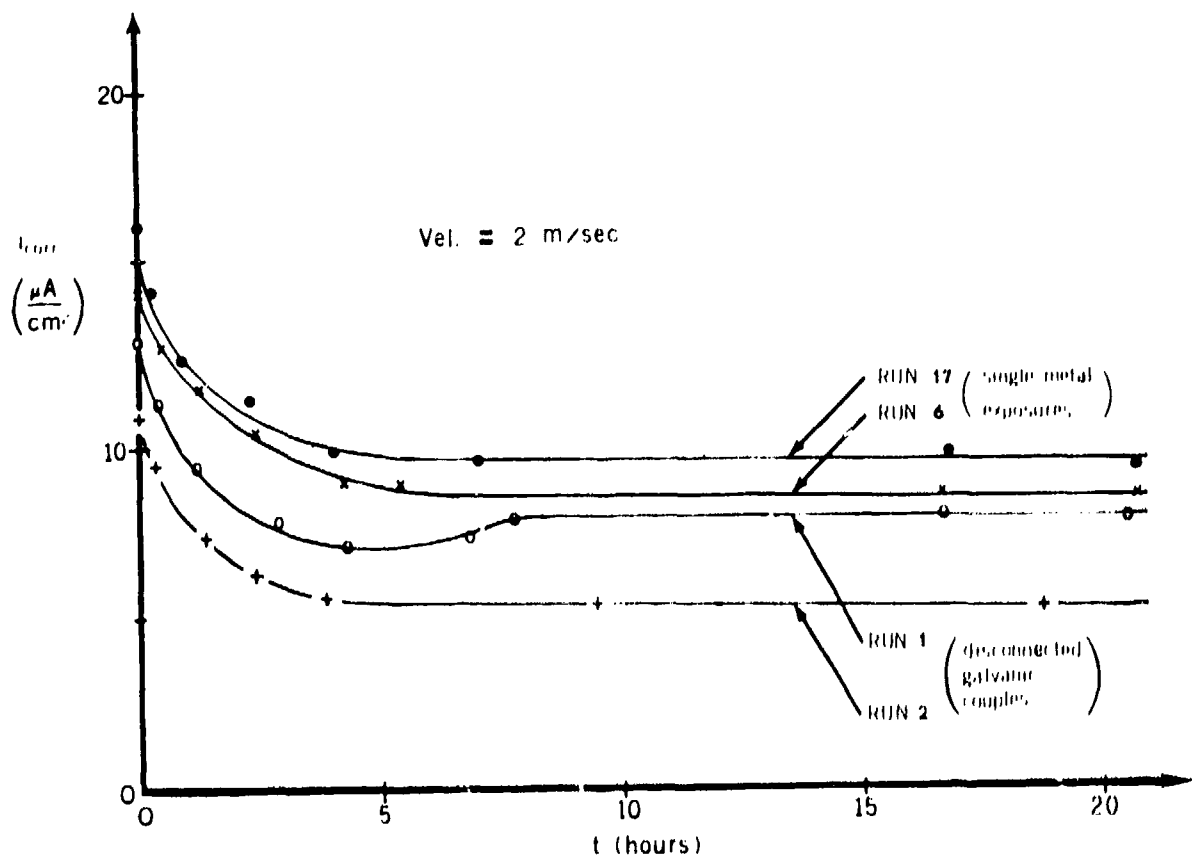


Figure 16: LPM-determined corrosion rates versus time for 90/10 Cu-Ni at 2 m/sec.

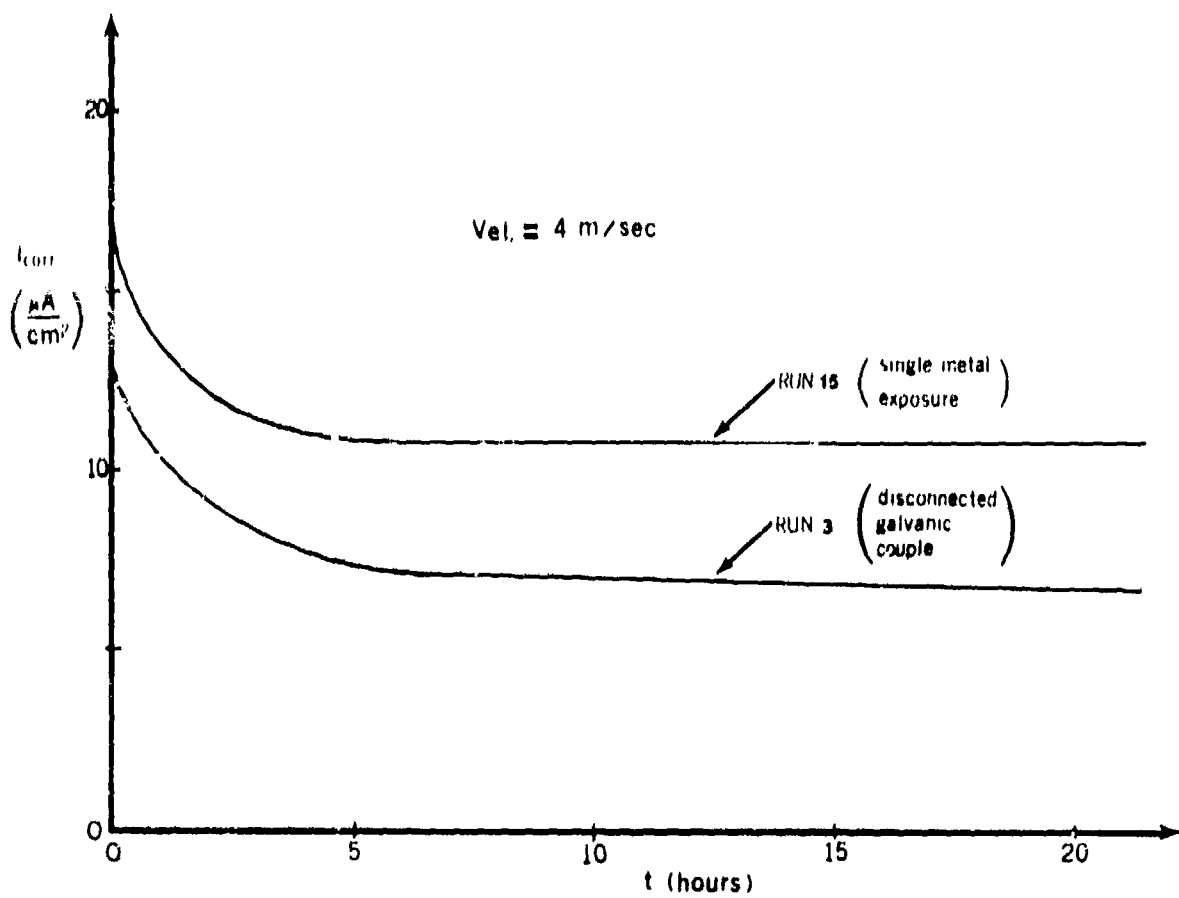


Figure 17: LPM-determined corrosion current density versus time for 90/10 Cu-Ni at 4 m/sec.

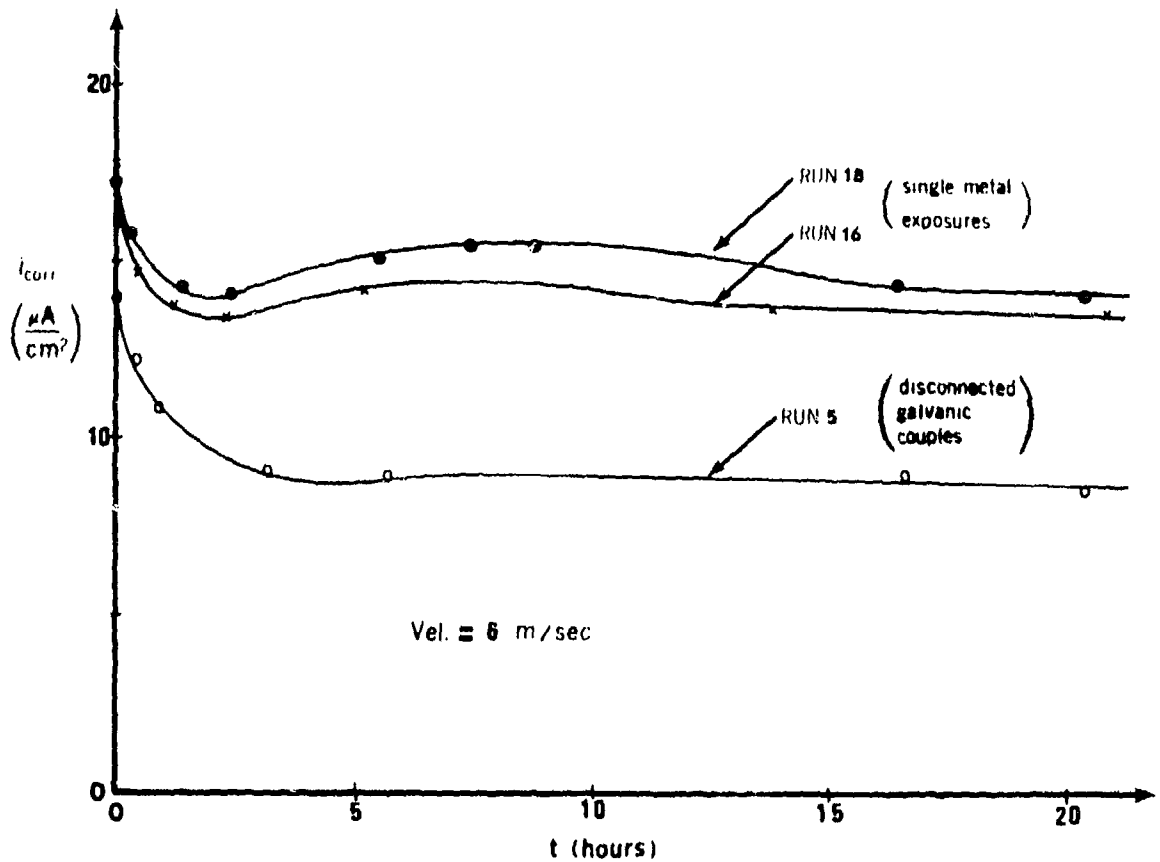


Figure 18: LPM-determined corrosion current density versus time for 90/10 Cu-Ni at 6 m/sec.

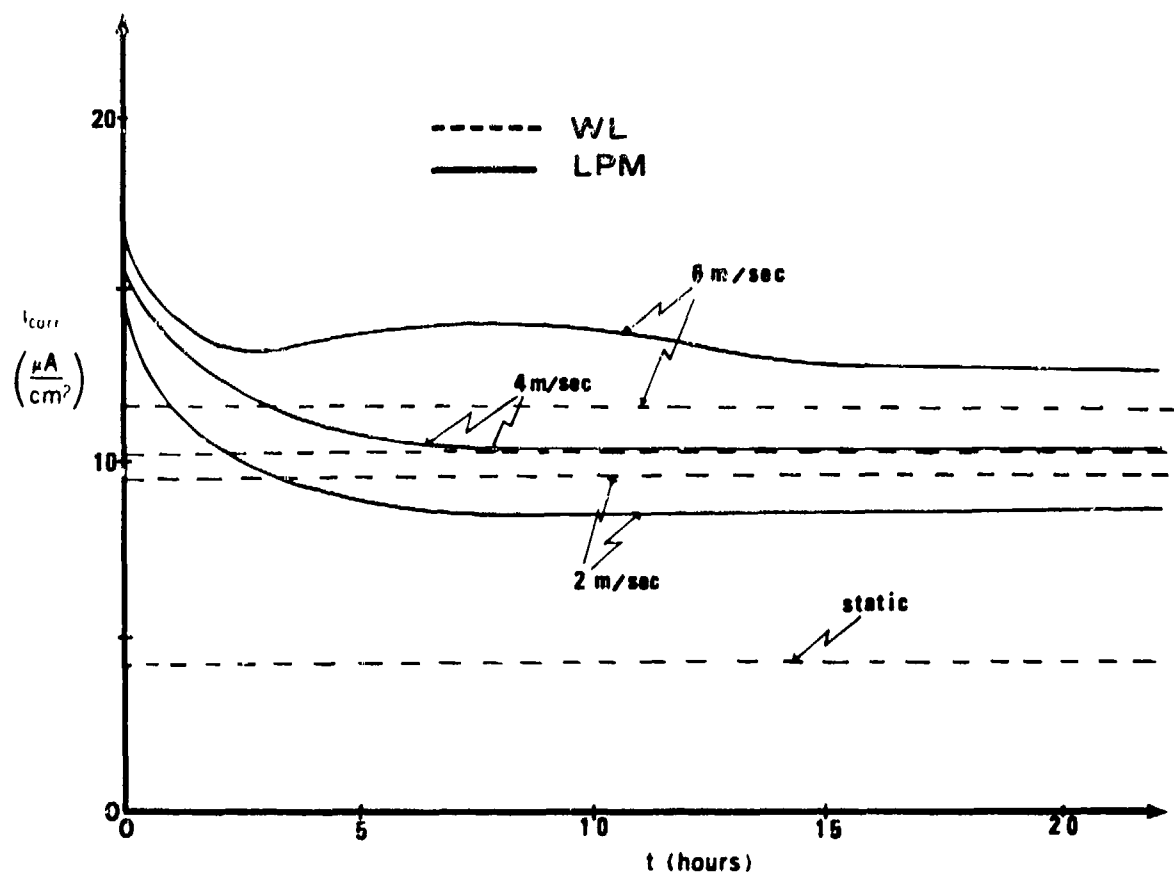


Figure 19: Comparison of the LPM-determined corrosion current density and the WL-determined apparent average corrosion current density for 90/10 Cu-Ni at 2, 4, and 6 m/sec.

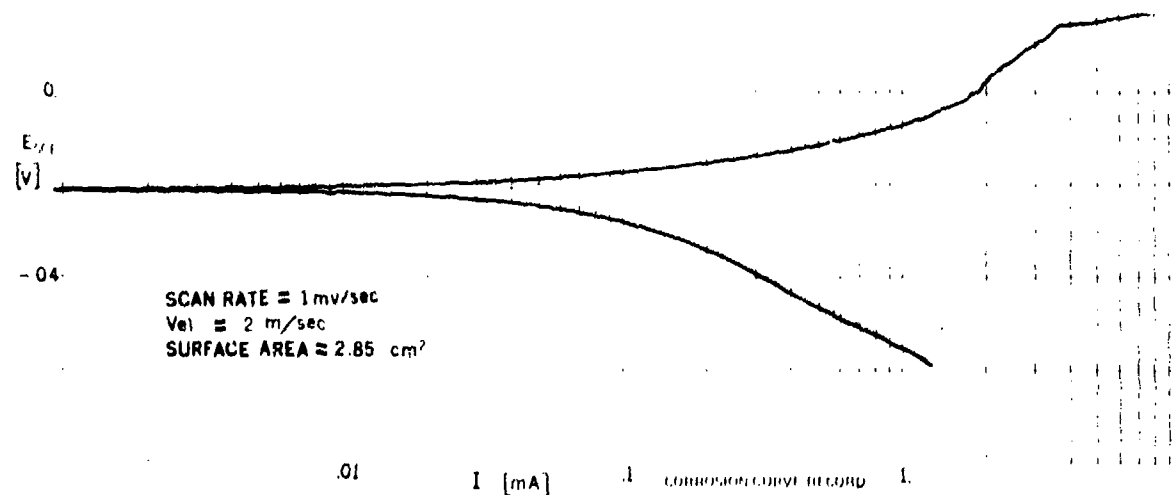


Figure 20: Potentiodynamic polarization curve for 90/10 Cu-Ni at 2 m/sec.
Sample surface area = 2.85 cm².

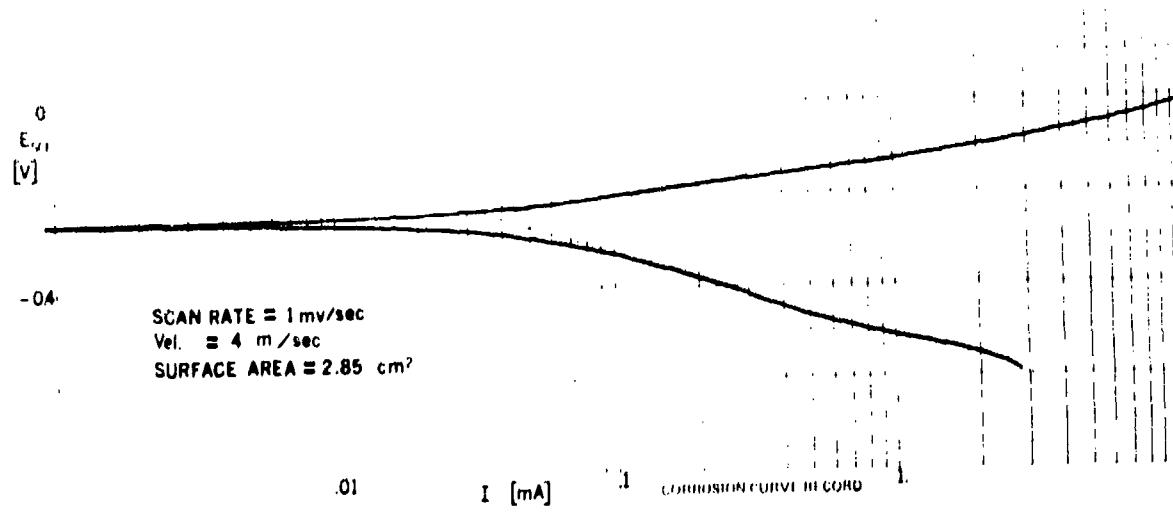


Figure 21: Potentiodynamic polarization curve for 90/10 Cu-Ni at 4 m/sec.
Sample surface area = 2.85 cm².

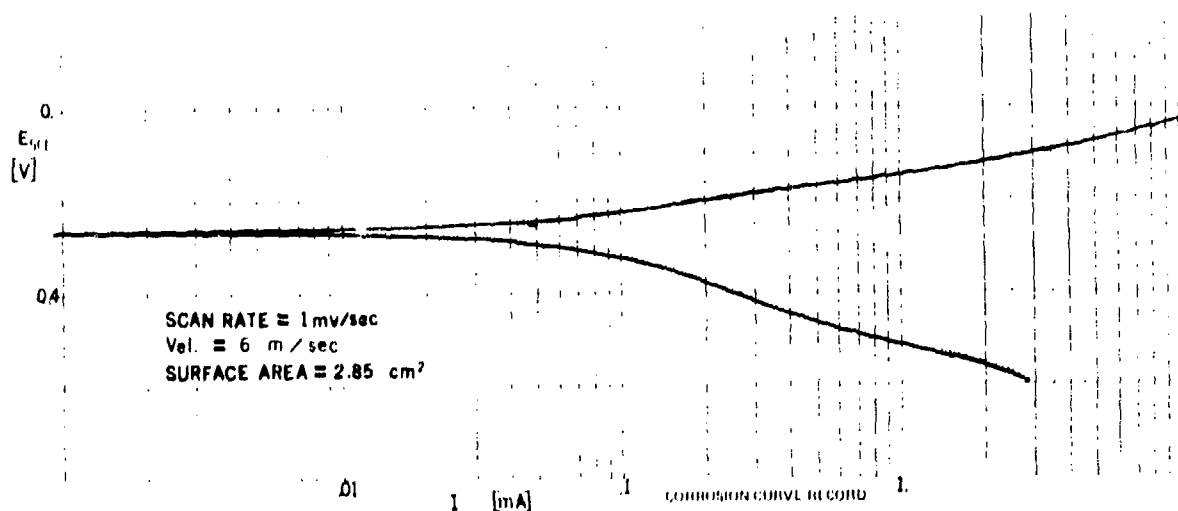


Figure 22: Potentiodynamic polarization curve for 90/10 Cu-Ni at 6 m/sec.
Sample surface area = 2.85 cm².

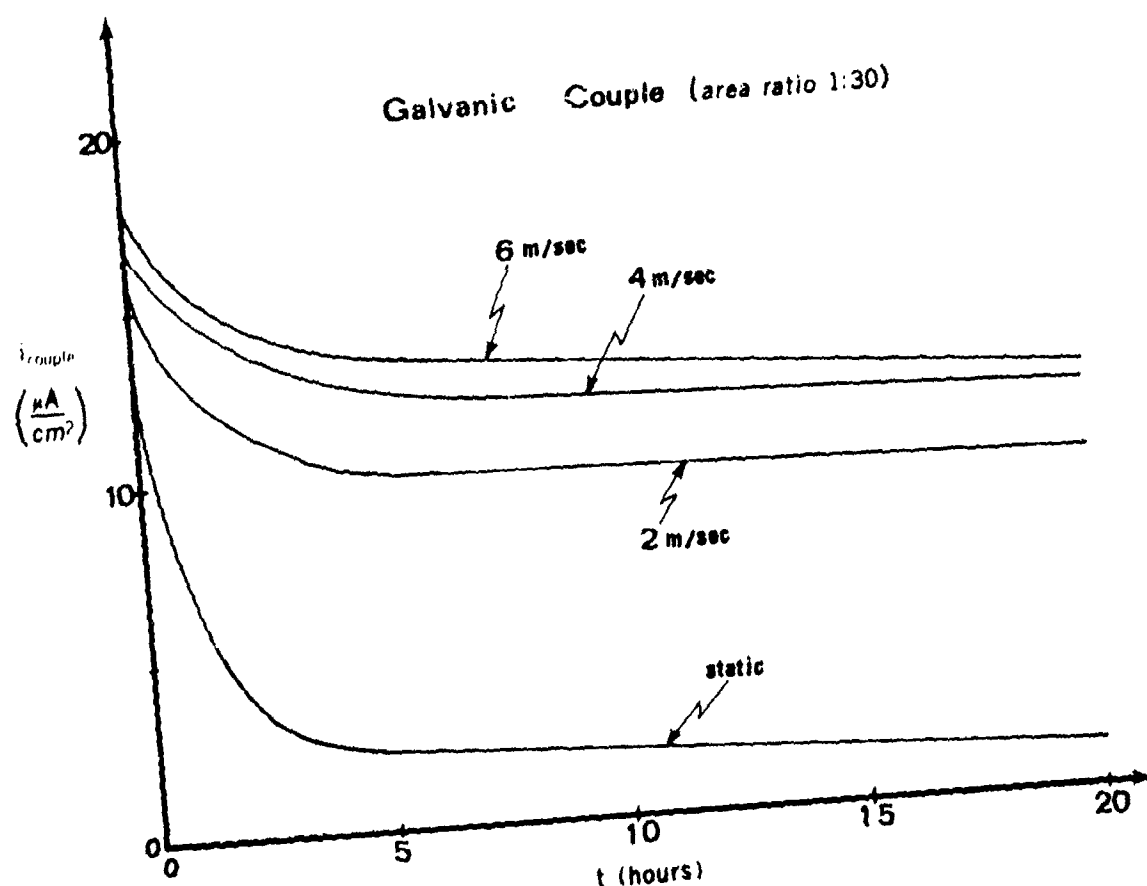


Figure 23: ZRA-determined galvanic current density versus time for 90/10 Cu-Ni:
Pt (area ratio 1:30) couples at 0, 2, 4, and 6 m/sec.

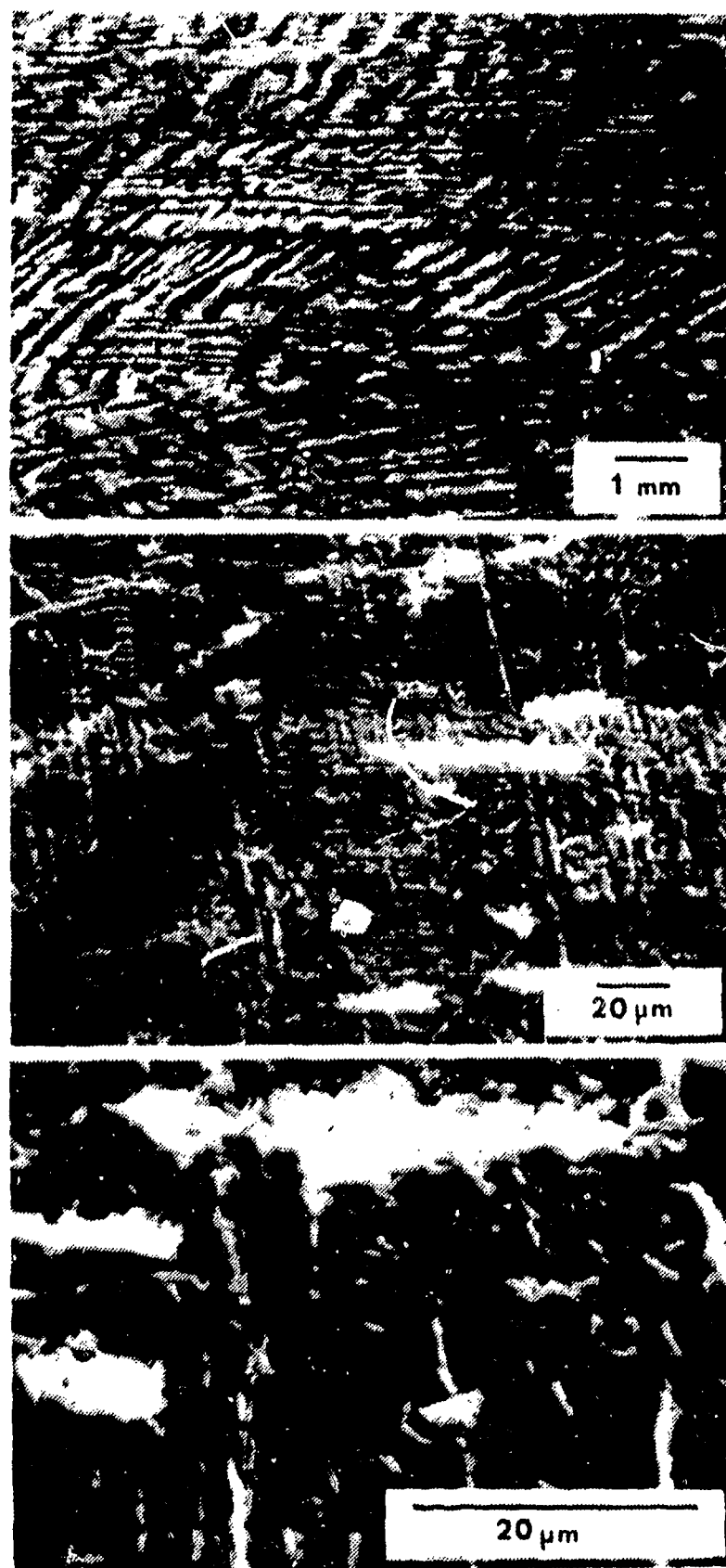


Figure 24: As-exposed surface of 90/10 Cu-Ni sample after 24 hr. exposure in galvanic couple with Pt (area ratio 1:30) at 6 m/sec. (a) Light micrograph, 10X, (b) SEM micrograph, 500X, (c) SEM micrograph, 2000X.

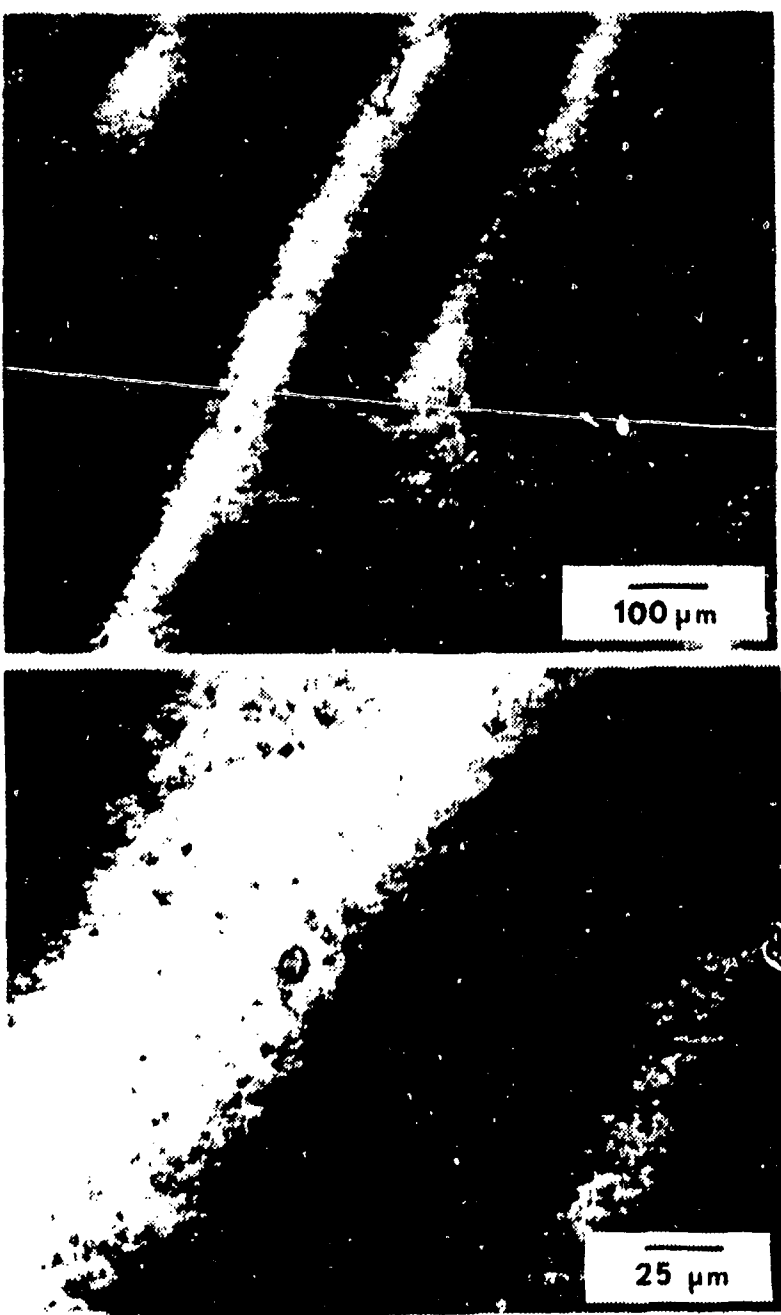


Figure 25: As-exposed surface of 90/10 Cu-Ni sample after 24 hr. exposure in galvanic couple with Pt (area ratio 1:30) at 4 m/sec. Light micrographs (a) 100X, (b) 400X.

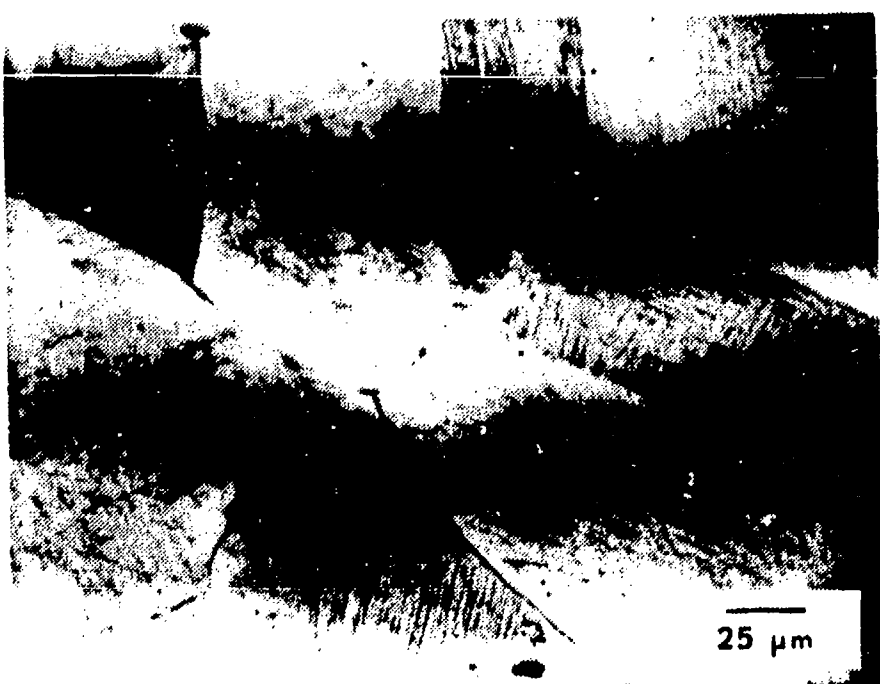


Figure 26: Polished and etched metallographic view of the microstructure of the 90/10 Cu-Ni sample material, 400X.

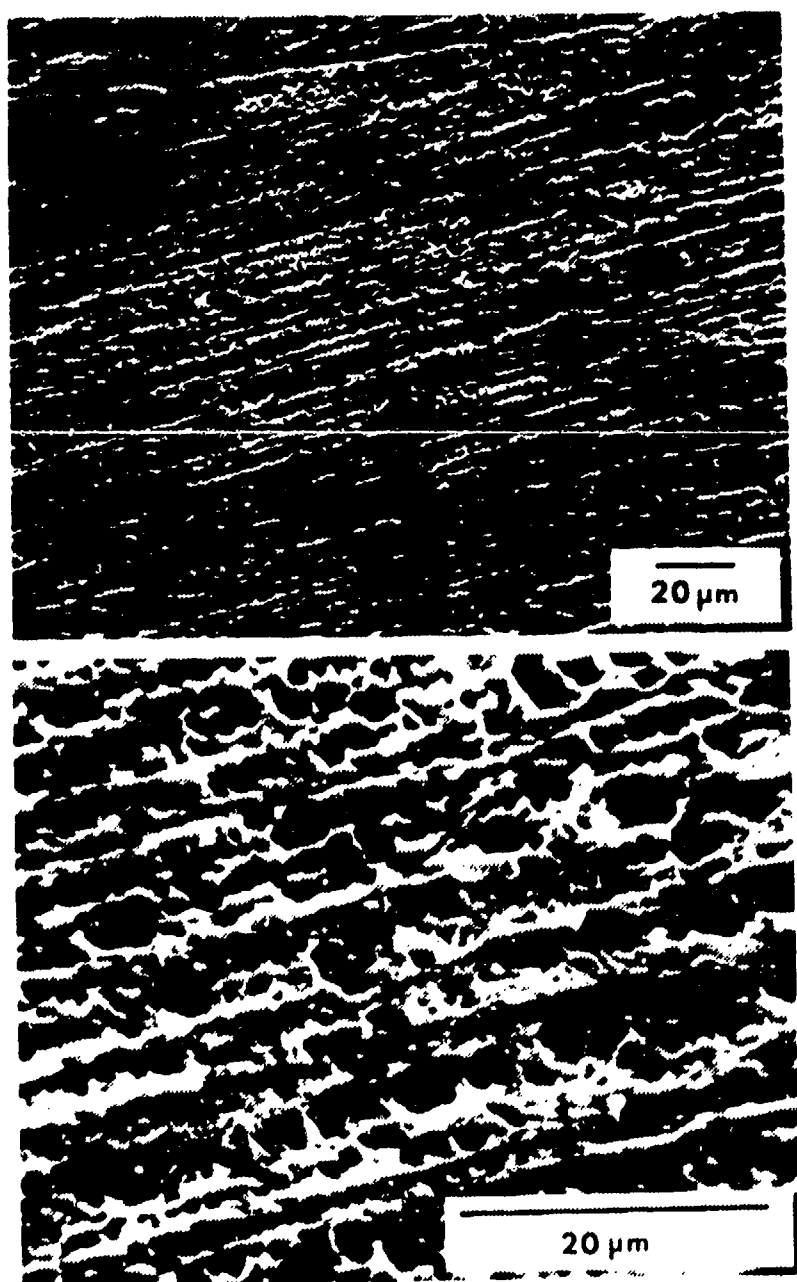


Figure 27: SEM view of cleaned surface of 90/10 Cu-Ni sample after 24 hour exposure in galvanic couple with Pt (area ratio 1:30) at 6 m/sec (a) 500X, (b) 2000X

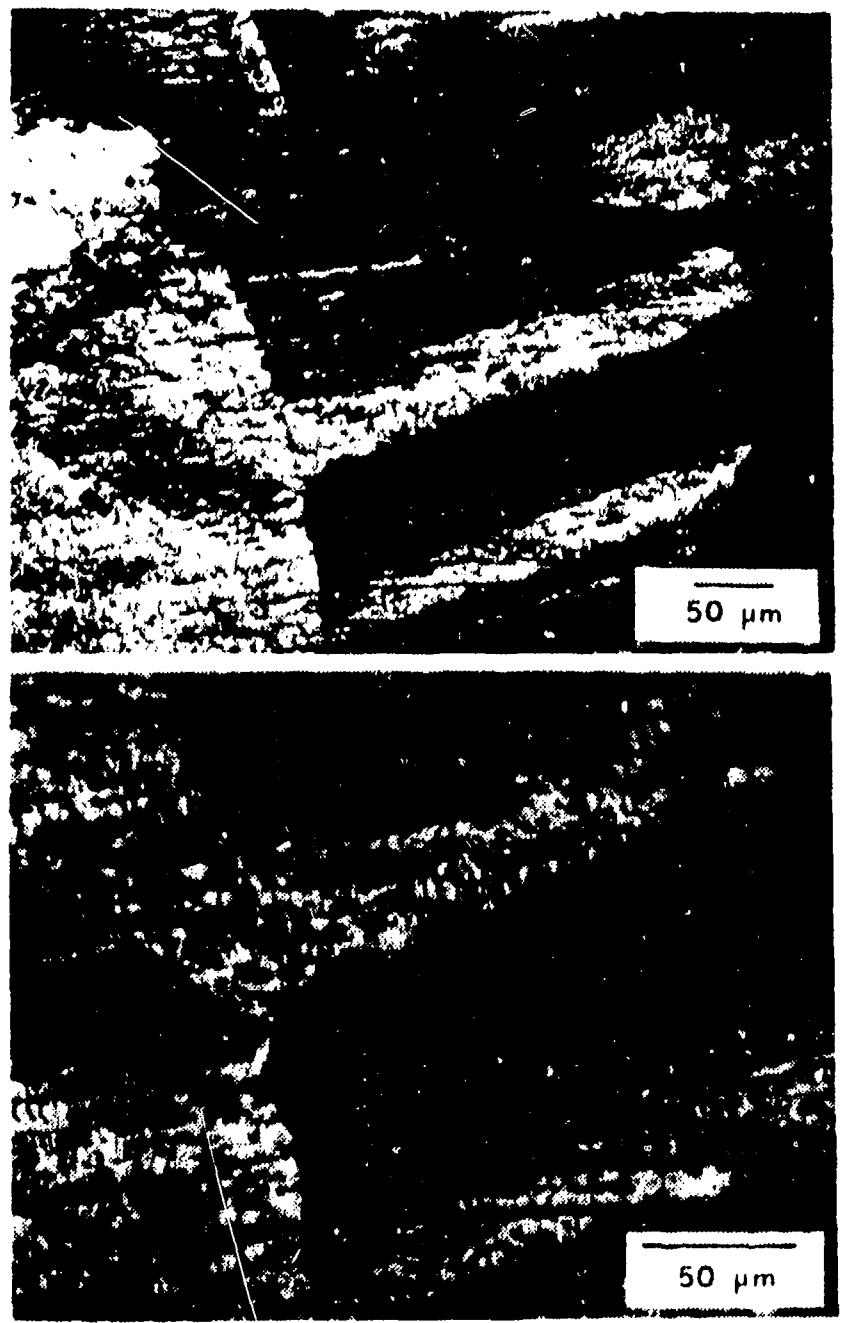


Figure 28: Light microscope views of cleaned surface of 90/10 Cu-Ni sample after 24 hour exposure in galvanic couple with Pt (area ratio at 4 m/sec., (a) 100x, (b) 400x)

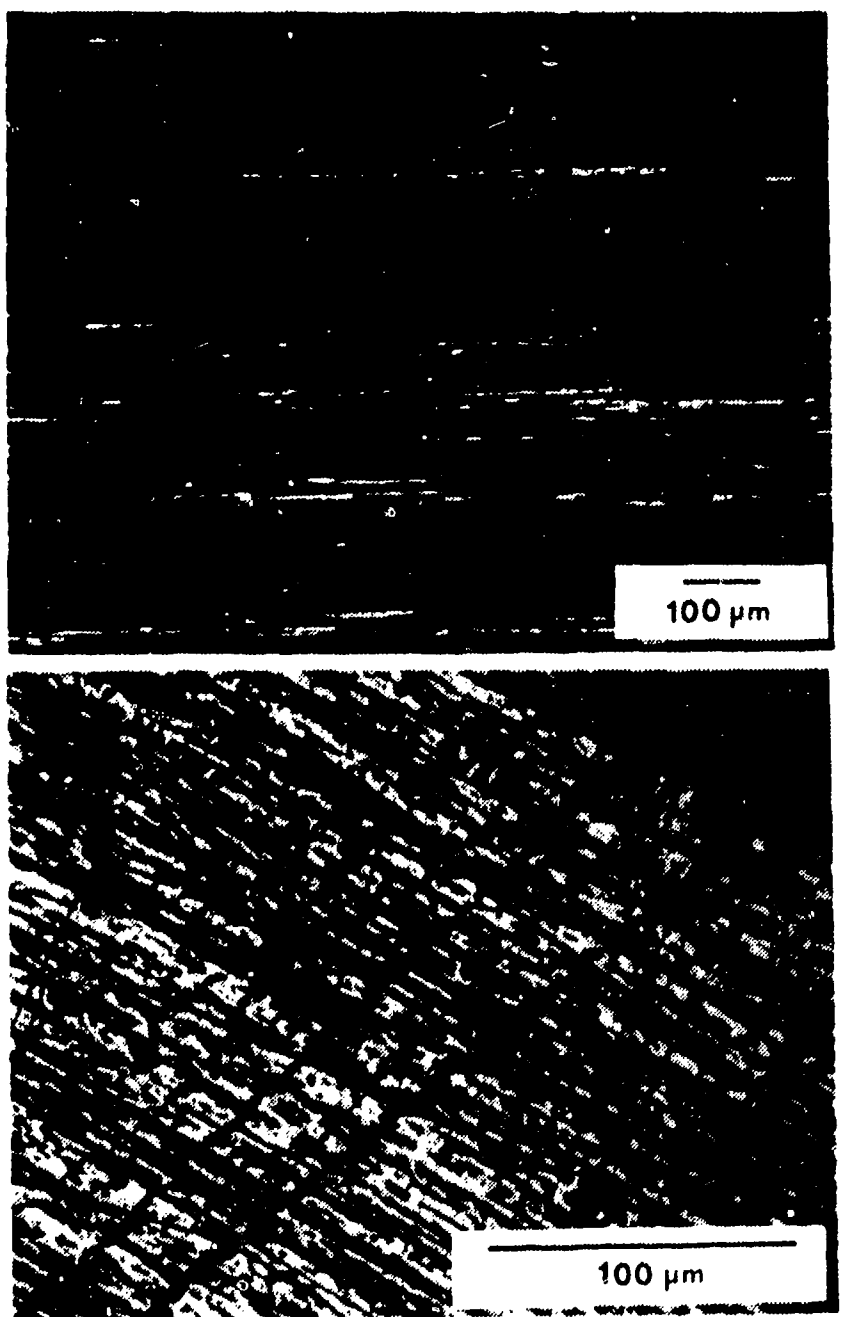


Figure 29: Cleaned surfaces of samples of 90/10 Cu-Ti after single metal exposures for 24 hours at (a) 6 m/sec, 100X, (b) 2 m/sec, 400X. Light microscope views.

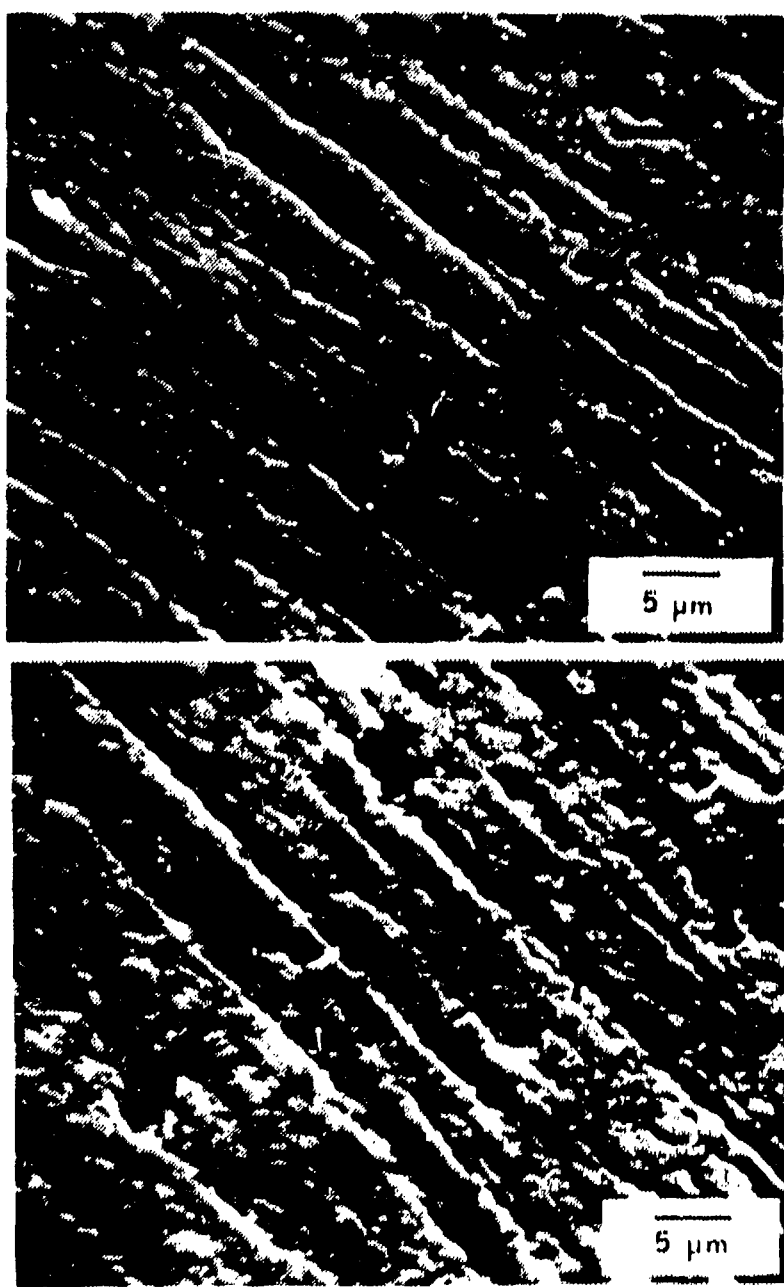


Figure 30: SEM views of cleaned surfaces of 90/10 Cr/Fe samples after single metal exposure for 48 hours at (a) 2 m/sec., (b) 6 m/sec. Both 7000x.

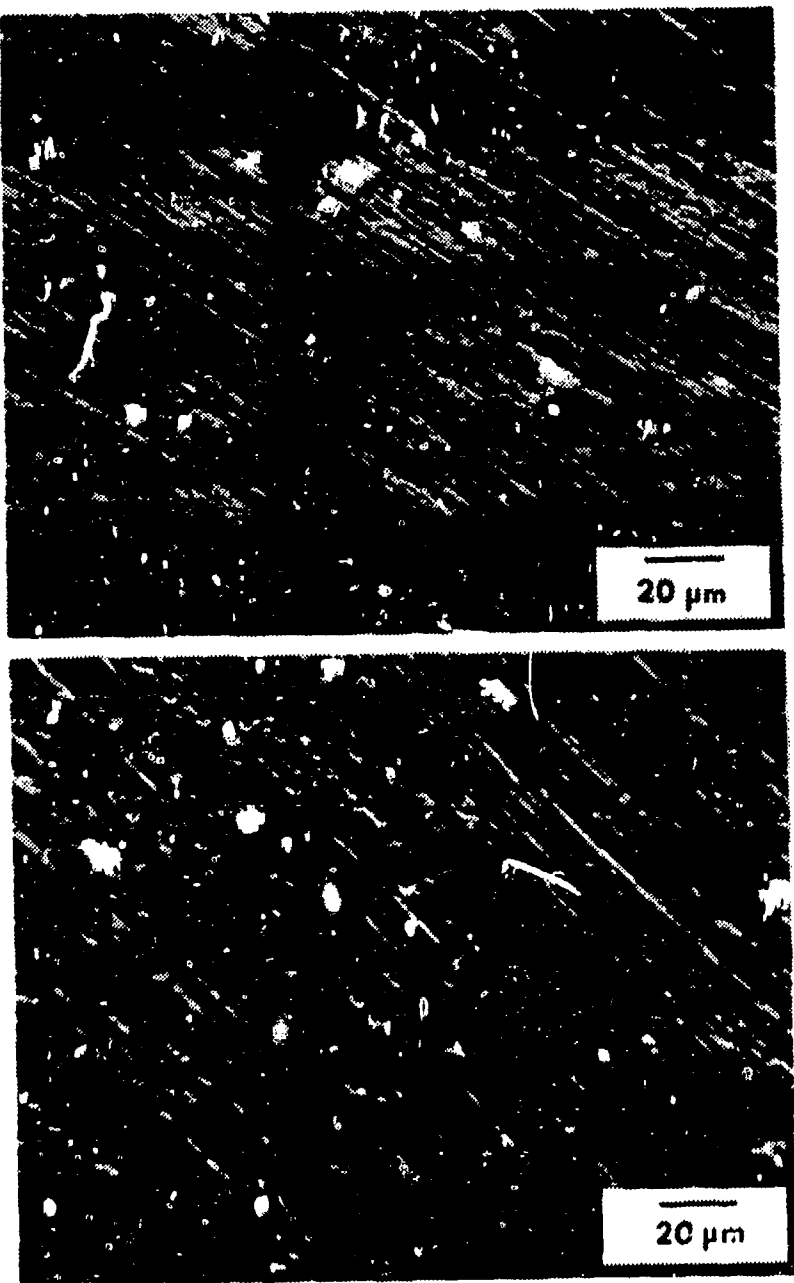


Figure 31: SEM views of cleaned surfaces of 90/10 Cu-Ni samples after single metal exposures for 48 hours at (a) 2 m/sec, (b) 6 m/sec. Both 500X.

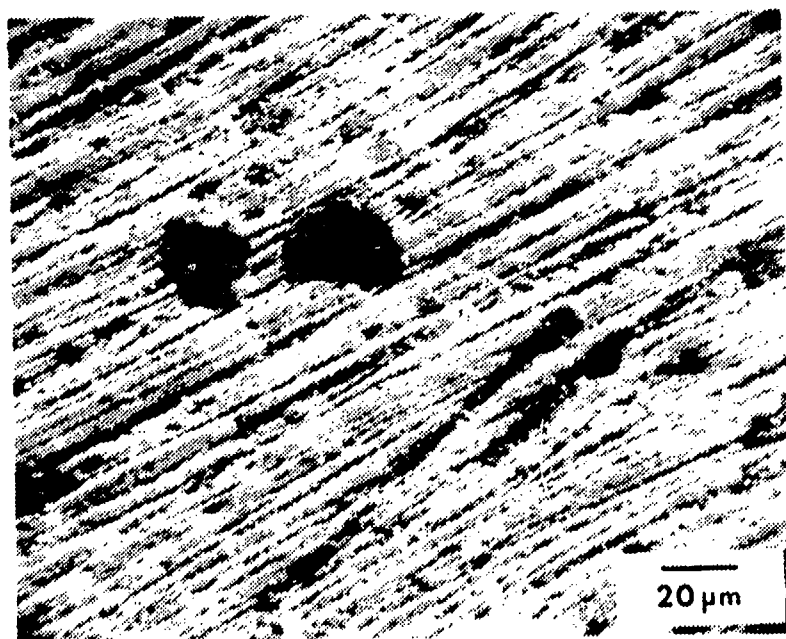


Figure 32: SEM view of as-exposed surface of 90/10 Cu-Ni single metal.
Sample after static exposure for 72 hours. 500X.

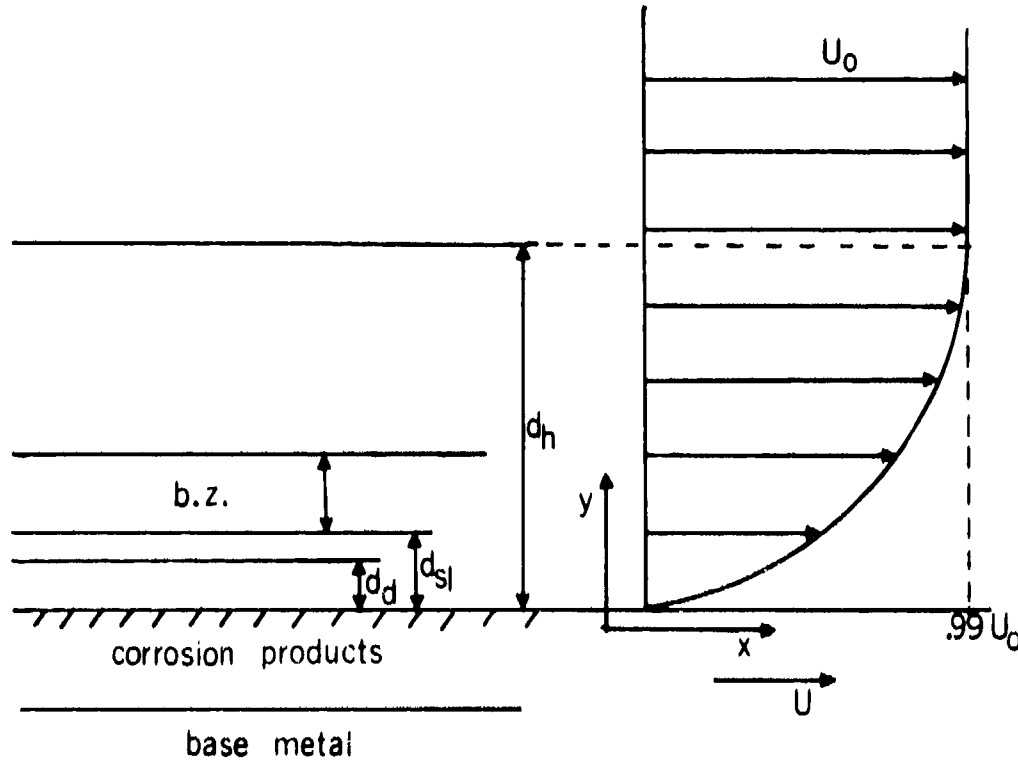


Figure 33: Schematic of boundary layers in turbulent flow, and the velocity profile across the boundary layers.

d_h = hydrodynamic boundary layer

d_{s1} = viscous sublayer

b.z. = buffer zone

$d_h - b.z. - d_{s1}$ = turbulent region of boundary layer

d_d = diffusion boundary layer

U_0 = free stream relative velocity

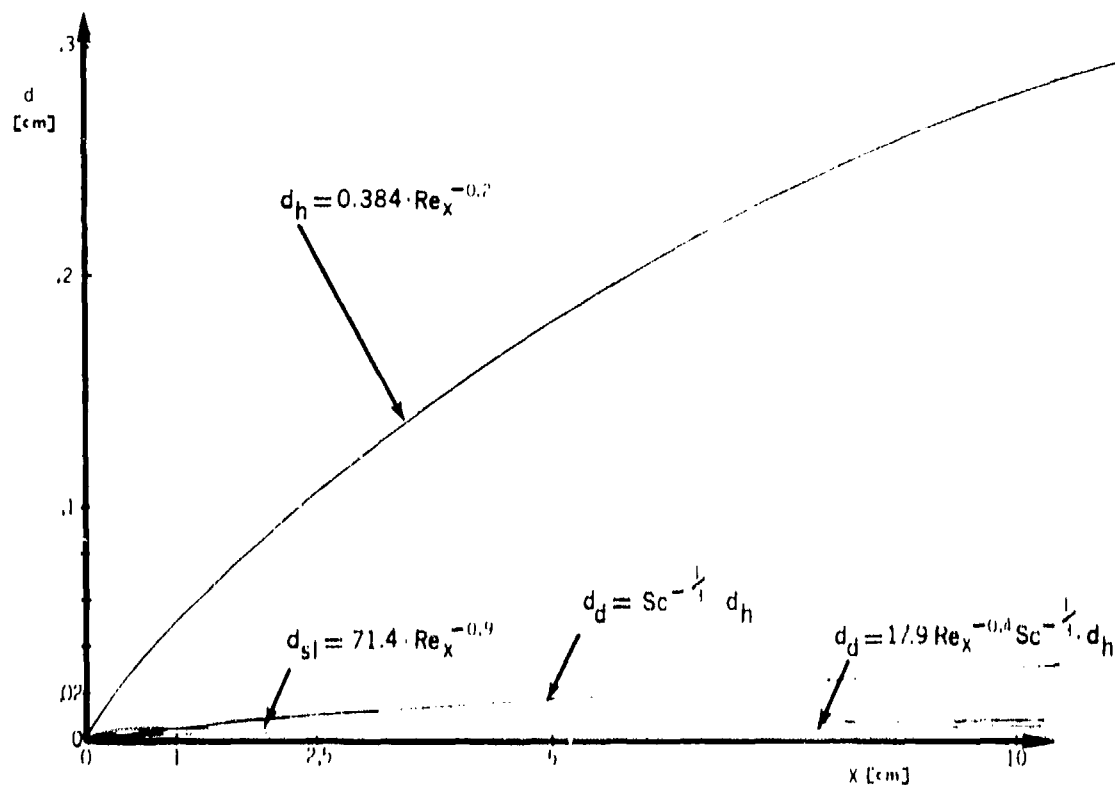


Figure 34: Calculated boundary layer development along a flat plate according to the indicated formulae.

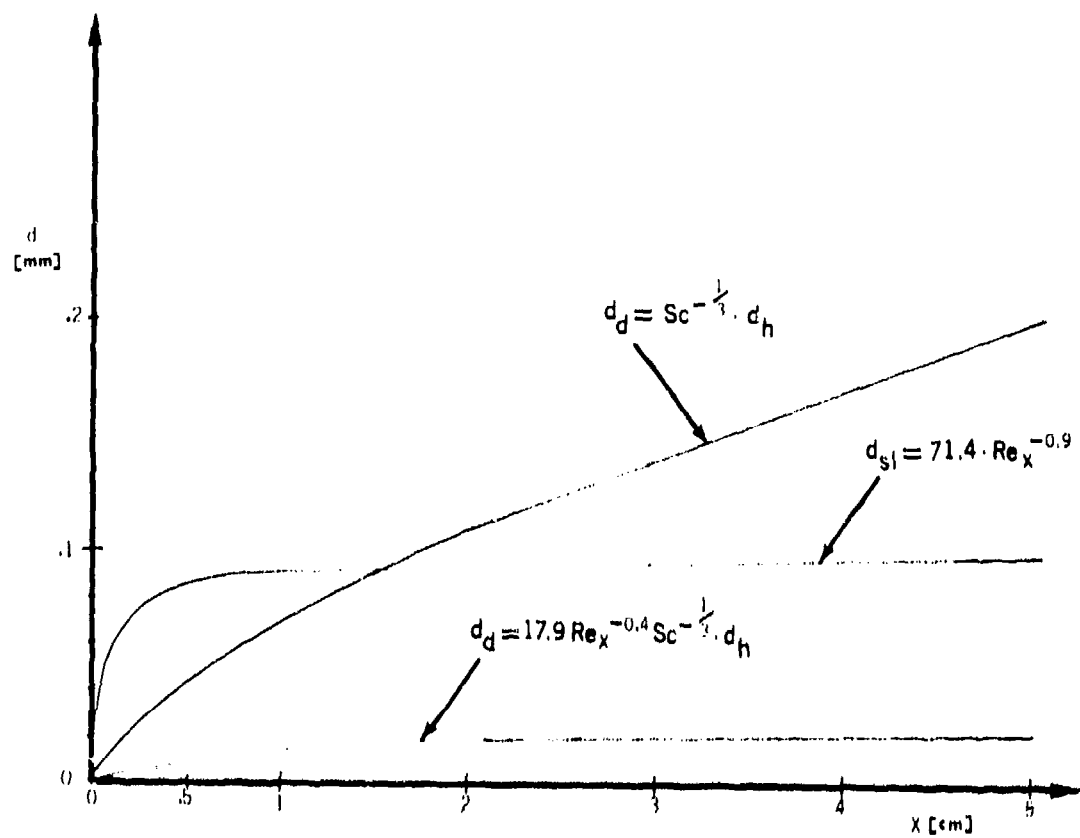


Figure 35: Calculated boundary layer development along a flat plate according to the indicated formulae. Scales expanded from those of Figure 34.

INITIAL DISTRIBUTION LIST

	<u>No. Copies</u>
1. Defense Documentation Center Cameron Station Alexandria, Virginia 22314	2
2. Library, Code 0142 Naval Postgraduate School Monterey, California 93940	2
3. Department Chairman, Code 69 Department of Mechanical Engineering Naval Postgraduate School Monterey, California 93940	2
4. Naval Research Laboratory Washington, D. C. 20390 Code 2627	1
5. Naval Air Propulsion Test Center Trenton, NJ 08628 Attn: Library	1
6. Office of Naval Research Department of the Navy (Attn:Code 471) 800 N. Quincy Street Arlington, VA 22217	1
7. Naval Air Development Center Code 302 Warminster, PA 18974 Attn: Mr. F. S. Williams	1
8. Naval Construction Battalion Civil Engineering Laboratory Port Hueneme, CA 93043 Attn: Materials Division	1
9. Office of Naval Research 800 N. Quincy Street Arlington, VA 22217 Attn: Code 102	1
10. Naval Electronics Lab. Center San Diego, CA 92152 Attn: Electron Materials Sciences Division	1
11. Naval Materials Center Materials Consultant Code 3312-1 Point Mugu, CA 93041	1

12. Office of Naval Research 800 N. Quincy Street Arlington, VA 22217 Attn: Code 470	1
13. Commanding Officer Naval Surface Weapons Center White Oak Laboratory Silver Spring, MD 20910	1
14. David W. Taylor Naval Ship R & D Center Materials Department Annapolis, MD 21402	1
15. Commanding Officer Office of Naval Research Branch Office 495 Summer Street Boston, MA 02210	1
16. Naval Undersea Center San Diego, CA 92132 Attn: Library	1
17. Naval Underwater System Center Newport, RI 02840 Attn: Library	1
18. Commanding Officer Office of Naval Research Branch Office 536 S. Clark Street Chicago, IL 60605	1
19. Naval Weapons Center China Lake, CA 93555 Attn: Library	1
20. Naval Air Systems Command Washington, D. C. 20360 Attn: Code 52031	1
21. Office of Naval Research San Francisco Area Office 760 Market Street, Rm 447 San Francisco, CA 94102	1
22. Naval Air Systems Command Washington, D. C. Attn: Code 52032	1
23. Naval Air Systems Command Washington, D. C. 20360 Attn: Code 320	1

24.	Naval Research Lab. Washington, DC 20390 Attn: Code 6000	1
25.	Naval Sea System Command Washington, DC 20362 Attn: Code 035	1
26.	NASA Headquarters Washington, D. C. Attn: Code RRM	1
27.	Naval Research Lab. Washington, DC 20390 Attn: Code 6100	1
28.	Naval Facilities Engineering Command Alexandria, VA 22331 Attn: Code 03	1
29.	NASA Lewis Research Center 20111 Brookpark Road Cleveland, Ohio 44135 Attn: Library	1
30.	Naval Research Lab. Washington, D.C. 20390 Attn: Code 6300	1
31.	Scientific Advisor Commandant of the Marine Corps Washington, D. C. 20380 Code AX	1
32.	National Bureau of Standards Washington, DC 20234 Attn: Metallurgy Division Inorganic Mat. Div.	1
33.	Dr. Wm. R. Prindle National Academy of Sciences National Research Council 2101 Constitution Ave. Washington, DC 20418	1
34.	Dr. R. P. Wei, Lehigh Univ. Inst. for Fracture & Solid Mechanics Bethlehem, PA 18015	1
35.	Prof. H. G. F. Wendorff Univ. of Virginia Dept. of Mat. Science Charlottesville, VA 22903	1

36. Defense Metals and Ceramics Info Center Battelle Mem. Institute 505 King Ave. Columbus, Ohio 43201	1
37. Naval Ship Engr. Center CTR BG #2 Code 6101 3700 E-W Highway Prince George Plaza Hyattsville, MD 20782	1
38. Director, Ordnance Research Lab. P.O. Box 30 State College, PA 16801	1
39. Army Research Office Box CM, Duke Station Durham, NC 27706 Attn: Metallurgy & Cer. Div.	1
40. Army Materials and Mechanics Research Center Watertown, MA 02172 Attn: (AMXMR-P)	1
41. Dir. Applied Physics Lab. University of Washington 1013 NE 40th Street Seattle, WA 98105	1
42. Metals and Ceramics Div. Oak Ridge Nat'l Lab. P.O. Box X Oak Ridge, TN 37380	1
43. AF/Ofc. of Scientific Research Bldg. 410 Bolling AF Base Washington, D. C. 20332 Attn: Chem. Sci. Directorate Electronics & S. S. Sci. Director	1
44. Los Alamos Scientific Lab P.O. Box 1663 Los Alamos, NM 87544 Attn: Report Librarian	1
45. AF Materials Lab. (LA) Wright-Patterson AFBaSe Dayton, Ohio 45433	1
46. Argonne National Lab. Metallurgy Division P.O. Box 229 Lemont, IL 60439	1

47. Dr. J. A. S. Green 1
 Martin Marietta Corp.
 1450 S. Rolling Road
 Baltimore, MD 21227

48. Dr. T. R. Beck 1
 Electrochemical Tech. Corp.
 10035 31st Ave. NE
 Seattle, WA 98125

49. Prof. R. H. Heidersbach 1
 University of Rhode Island
 Department of Ocean Engr.
 Kingston, RI 02881

50. Professor I. M. Bernstein 1
 Carnegie-Mellon Univ.
 Schenley Park
 Pittsburgh, PA 15213

51. Professor H. K. Birnbaum 1
 Univ. of Illinois
 Dept. of Metallurgy
 Urbana, IL 61801

52. Prof. J. P. Hirth 1
 Ohio State University
 Metallurgical Engineering
 Columbus, OH 43210

53. Prof. H. Herman 1
 State Univ. of New York
 Materials Science Div.
 Stony Brook, NY 11794

54. Dr. Otto Buck 1
 Rockwell International
 1049 Camino Del Rio
 P.O. Box 1085
 Thousand Oaks, CA 91360

55. Dr. D. W. Hoepplner 1
 University of Missouri
 College of Engineering
 Columbia, MO 65201

56. Prof. H. W. Pickering 1
 Pennsylvania State Univ.
 Dept. of Mat. Sciences
 University Park, PA 16802

57. Dr. David L. Davidson 1
 Southwest Research Inst.
 8500 Gilead Road
 P.O. Drawer 28510
 San Antonio, TX 78284

58. Dr. E. W. Johnson 1
 Westinghouse Electric Corp.
 Research and Development Center
 1310 Beulah Road
 Pittsburgh, PA 15235

59. Dr. F. Mansfeld 1
 Rockwell
 1049 Camino Dos Rios
 P.O. Box 1085
 Thousand Oaks, CA 91360

60. Dr. D. J. Duquette 1
 Dept. of Metallurgical Engr.
 Rensselaer Polytechnic Inst.
 Troy, NY 12181

61. Prof. R. T. Foley 1
 The American University
 Dept. of Chemistry
 Washington, DC 20016

62. Prof. A. E. Miller 1
 University of Notre Dame
 College of Engineering
 Notre Dame, IN 46556

63. Mr. G. A. Gehring 1
 Ocean City Research Corp.
 Tennessee Ave. & Beach Thorofare
 Ocean City, NJ 08226

64. Prof. R. W. Staehle 1
 Ohio State University
 Dept. of Metallurgical Engr.
 Columbus, OH 43210

65. Dr. Barry C. Syrett 1
 Stanford Research Institute
 333 Ravenswood Avenue
 Menlo Park, CA 94025

66. Brookhaven Nat'l Laboratory 1
 Technical Info. Div.
 Upton, LI
 New York 11973
 Attn: Research Library

67. Library 1
 Building 50 Rm 134
 Lawrence Radiation Laboratory
 Berkeley, CA 94550

68. Prof. Jeff Perkins 30
 Naval Postgraduate School
 Code (69Pn)
 Monterey, CA 93940